Micro-mechanical Analysis of Pile Installation Methods

Wenchu Du

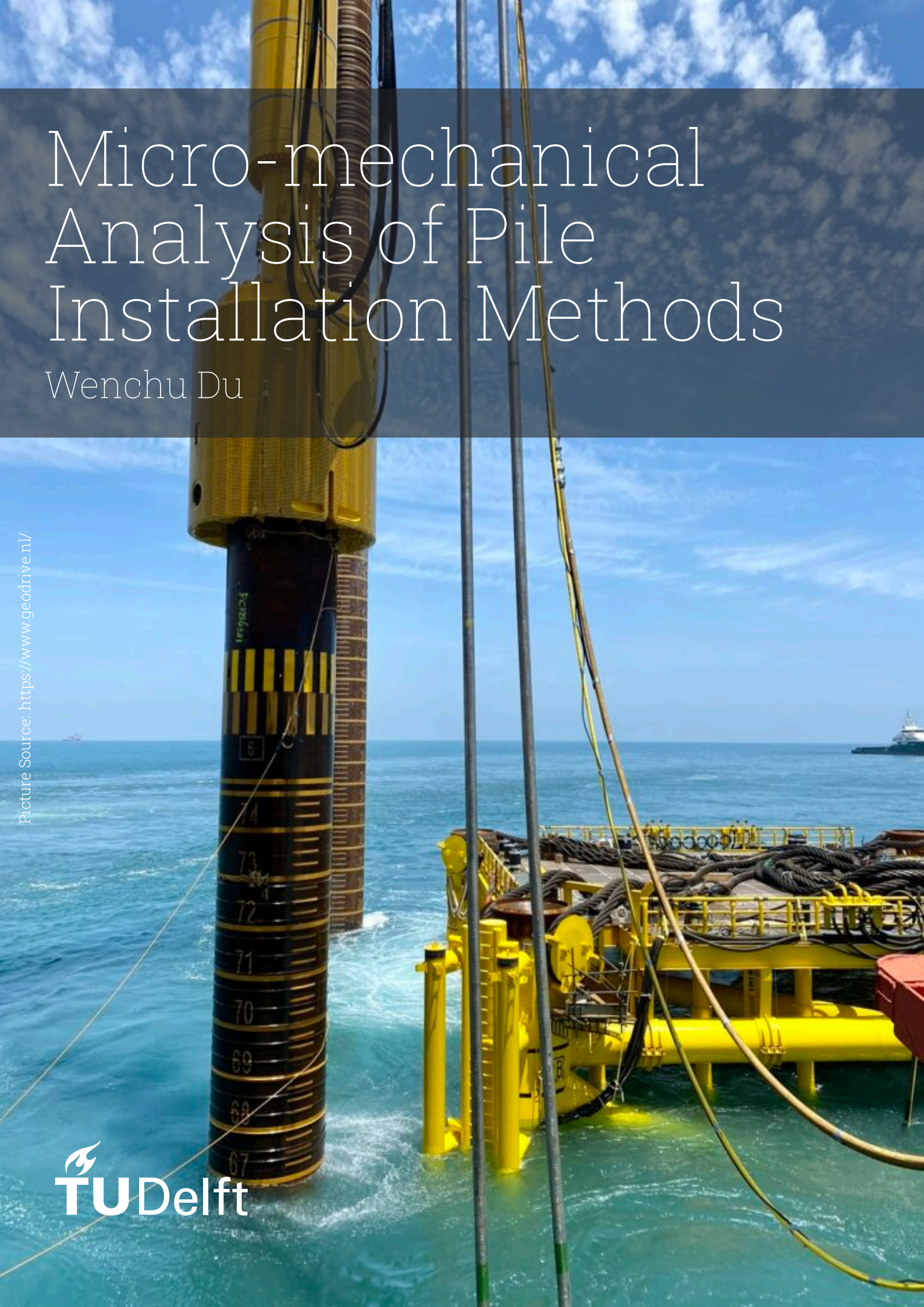

Picture Source: https://www.geodrive.nl/

TU Delft

Micro-mechanical Analysis of Pile Installation Methods

by

Wenchu Du

to obtain the degree of Master of Science
at the Delft University of Technology,
to be defended publicly on Friday August 15, 2025 at 14:00 PM.

Student number:	5914701	
Project duration:	November 1, 2024 – August 15, 2025	
Thesis committee:	Miguel Angel Cabrera	TU Delft, supervisor
	Martin Lesueur	TU Delft
	Luca Flessati	TU Delft

TU Delft

Preface

The preparation of this thesis marks the achievement of my Master of Science studies in Civil Engineering at Delft University of Technology. This research, focused on the micro-mechanical investigation of pile installation methods, has allowed me to bridge theoretical knowledge and computational modeling in the context of geotechnical engineering. By exploring different installation techniques including jacking, impact driving, and vibratory driving, and investigating the factors that influence pull-out capacity through Discrete Element Method (DEM) simulations, this study sheds light on the soil-structure interactions that govern installation and pull-out efficiency as well as soil behavior during these processes.

During this 9-month work, I had overcome tons of difficulties. At the beginning of my thesis journey, even though I had some knowledge of DEM, I never used LMGC90 software, which made it extremely difficult for me to study from zero. After about 2 months of learning this new software, I started my first trial of building small-scale models to train my usage of it. In early February, I officially started my thesis work and the validation process of the model. However, due to the misunderstanding of particle size, I spent a really long period of time struggling with the computation time issue, which also made me extremely nervous at that time. Luckily, with the help of my supervisor and my own effort, the problem was finally solved and the thesis successfully came to an end. Even though this whole process was time-consuming and exhausting, it really helped me gain a lot, not only valuable knowledge about offshore pile foundation, DEM, advanced numerical methods, and computational mechanics; but it also cultivated my perseverance and the ability to solve problems.

At the end of this thesis, I would like to express my sincere thanks to some individuals. This work would not have been possible without their support. First and foremost, I would like to express my deep gratitude to my supervisor, Dr. Miguel Angel Cabrera, for his valuable guidance, constructive suggestions, and continuous encouragement throughout the project. I also thank Dr. Martin Lesueur and Dr. Luca Flessati for their technical advice and helpful discussions. Moreover, I am also thankful to Eli Hosseinzadeh Khaletabad and Laura Cote Martinez; their help in reviewing my thesis and post-processing of data really helped a lot. Also, thanks to Dr. Frederic Dubois and Dr. Rémy Mozul from Université de Montpellier who developed LMGC90; and Yihan Bai as well as other co-authors of the paper titled ”Penetration mechanism of open-ended pipe piles under jacking and driving methods” for providing additional information during my validation process.

In addition, I am grateful to my friends and classmates; I truly enjoyed every minute of the two years I spent with you. Your kindness, warmth, and help meant a lot to me, and I will always remember these two years and all of you. Also, I feel really lucky to have met my girlfriend Jiayi Wang, who kept supporting and encouraging me all the way along my thesis work; my ordinary life also became colorful because of you.

Finally, I would like to thank my family for their unwavering support and understanding during this demanding period. Along this 2-year trip in TU Delft, due to many reasons I had never been back to my family’s. I want to express my sincere apologies to them, and special thanks for their financial and mental support in my MSc study. I will always love you my whole life.

Wenchu Du
Delft, August 2025

Contents

1 Introduction

Today, when thinking about energy, there are multiple different choices: coal, oil, gas, nuclear, hydroelectric, solar, wind, and biomass. However, many of these energy sources are non-renewable, which means that once we run out of them, they cannot be reproduced within a couple of centuries, and most of these non-renewable energy sources will produce much pollution to the environment, leading to more serious pollution and the greenhouse effect. Comparing with non-renewable energy, one of the biggest advantages of renewable energy is the negligible contribution to the emissions of carbon dioxide, leaving a more sustainable Earth for next generations [1].

	Carbon Dioxide Emissions (t/GWh)
Coal	964
Oil	726
Gas	484
Nuclear	8
Wind	7
Photovoltaic	5
Large Hydro	4

Figure 1.1: Emissions of carbon dioxide for various power generation methods (taken from [2])

Looking back a few centuries, such as in Figure 1.7, we find that until 2023, we still relied mostly on natural gas, oil, and coal, which are non-renewable and high-polluting energy sources [3]. Only a small amount of energy used comes from wind energy.

The EU has long been committed to being a model leader in climate policy and governance and has implemented many climate mitigation policy measures [4]. In 2019, the EU launched the European Green Deal (EGD), which sets the EU on the path to a green transition, promising to reduce CO_2 emissions by 55% before 2030, with the ultimate goal of reaching climate neutrality by 2050 [5]. Offshore wind energy is at the heart of the strategy because of its huge potential to generate clean, sustainable electricity. In 2020, the European Commission published an integrated strategy for offshore renewables, setting a target of 60 GW of offshore wind capacity by 2030 to meet the strict climate targets set for 2030 and 2050 [6].

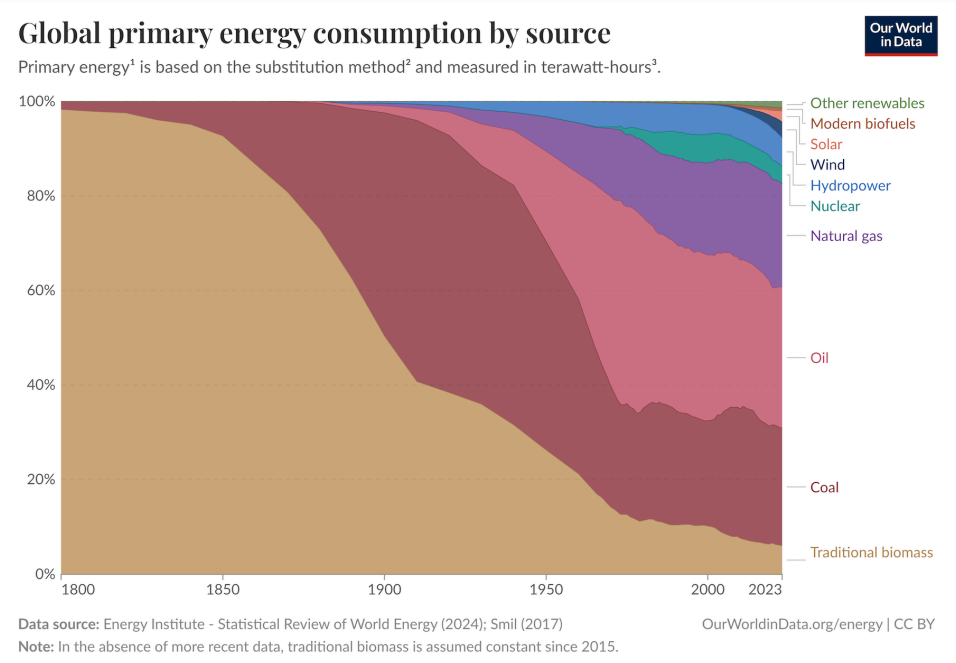

Figure 1.2: Global primary energy consumption by source (taken from [3])

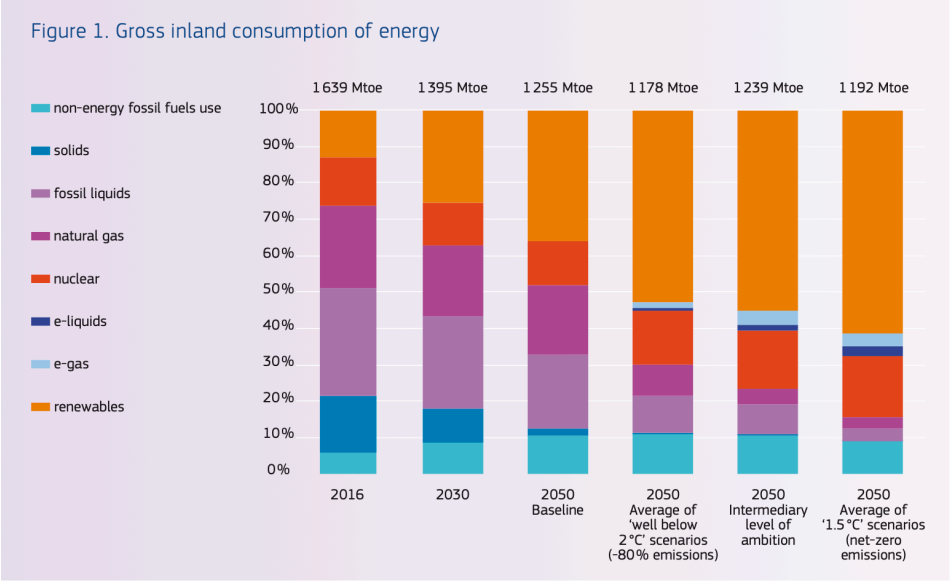

Figure 1.3: Percentages of different energy consumption sources in EU from 2016 to 2050 (taken from [7])

1.1. Pile foundation

Compared to onshore wind turbines, the biggest difference with offshore wind turbines is the foundation structure. How to deal with the interaction between the foundation and the environment, such as the loads brought by wind, waves, and even floating ice, puts higher requirements on the foundation design [8]. Nowadays, many different types of foundations have been implemented in the design of offshore wind turbines, such as monopile, jacket, suction bucket, etc [9]. The main types of foundations currently used and their respective advantages and disadvantages are shown in Table 1.1.

Table 1.1: Comparison of Offshore Foundation Types [10, 11, 12, 13, 14]

Foundation	Advantages	Disadvantages	Cost
Monopile	Simple design; cost-effective; industrialized production [10]	Limited to shallow water depths; prone to scour effects [10]	Low
Jacket	Suitable for deeper waters (up to 80 m); high structural adaptability [11]	High construction and installation costs [11]	High
Gravity	No need for piling; effective where piles cannot be driven [12]	Requires extensive seabed preparation; limited to shallow depths [12]	Medium
Suction Bucket	Efficient installation; suitable for medium water depths (up to 60 m); low environmental impact [13]	Not yet fully industrialized; limited experience in large-scale use [13]	Medium
Floating	Adaptable to the deepest waters; offers flexibility in positioning [14]	High operational movement; complex maintenance [14]	Very High

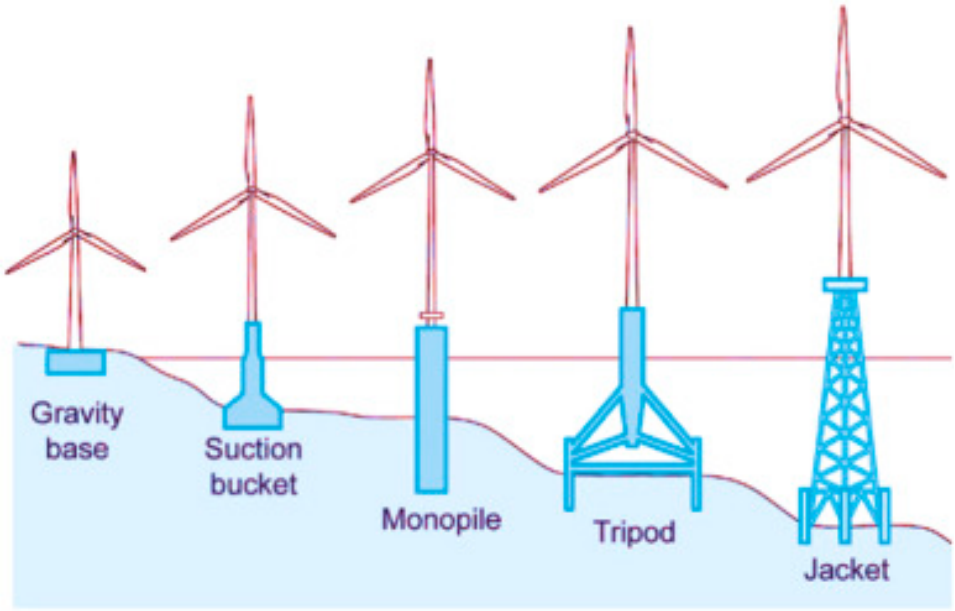

Figure 1.4: Schematic representation of offshore fixed foundation types. [15]

From Figure 1.4, it is clear that different foundation types are required for offshore wind turbines at different water depths. According to statistics, over 80% of foundation types are monopiles [16]. Monopile foundations offer simplicity, cost-effectiveness, and scalability, making them ideal for shallow to moderate-depth offshore wind farms with mature supply chains and efficient installation processes.

1.1.1. Monopile foundation

The monopile foundation consists of a large-diameter steel tubular structure driven into the seabed. Typically ranging from 3 to 6 meters in diameter, 20 to 50 meters in length, monopiles are designed to support the entire weight of offshore wind turbines [8]. Monopiles are especially effective in sandy seabeds, where the interaction between the pile and soil provides sufficient stability and strong enough support for the wind turbine.

The penetration resistance, which can be used to evaluate how much energy is needed for installing open-ended piles into soil layers, can be divided into two main parts: tip resistance and shaft friction. In order to save energy consumption as well as save construction time, finding an optimal pile installation

method for decreasing penetration resistance is necessary.

1.1.2. Pile installation methods

Offshore monopile installation is a non-standard operation due to the complexities involved [17]. Each monopile has unique requirements for installation, depending on factors such as pile diameter, operating environment, and available installation methods. As monopiles keep growing in diameter and weight, traditional installation techniques face significant challenges, including driving forces, base and shaft resistance, and deformation of the pile body and base soil. Thus, understanding and improving different installation methods are required to adapt to the growing demand for offshore wind turbines.

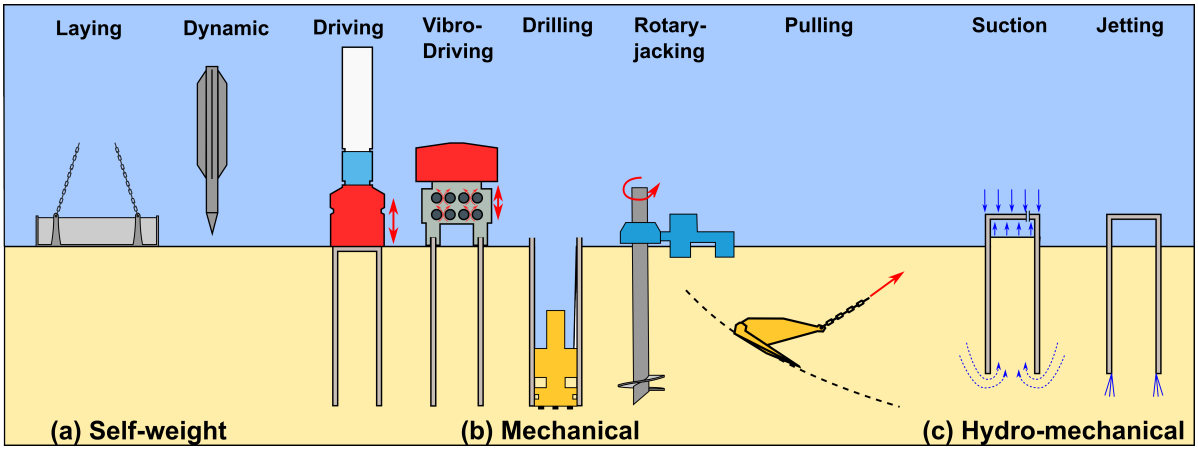

Figure 1.5: Offshore pile installation methods (taken from [18])

The most widely used installation method for monopile installation is impact driving. First, the monopile is transported from the manufacturing site to the installation location, using specialized vessels [19]. Once the monopile arrives, it is upended to a vertical position using cranes or upending tools. The monopile is then lowered into the water to its designated position on the seabed [20]. Subsequently, it is secured in place by impact driving, which involves using hydraulic hammers to embed the pile into the seabed, ensuring its stability.

Figure 1.6: Hydraulic impact hammer shown in red and white [21]

For some piles with a small diameter and light weight, or when the construction noise is supposed to

be strictly controlled, jacking is sometimes also used to install piles. The jacking method uses the pressure of a hydraulic jack to drive a prefabricated pile into a designed position. The soil will display during the jacking process. When the pile is driven into the ground, the displacement causes the surrounding soil to compress against the pile, thereby increasing the bearing capacity of the soil. Compared with other methods, jacking produces less vibration and noise and is less damaging to the pile body. It is also considered more environmentally friendly because it eliminates excavation work, thereby reducing the amount of waste and saving on site cleanup costs [22].

Nowadays, as people realize that traditional pile driving methods produce a lot of noise and cause great harm to marine life, vibratory pile driving is increasingly being used in engineering projects. Vibratory driving uses high-frequency vibrations to reduce the soil resistance around the pile, thereby driving the pile into the ground with minimal impact force [23]. The process involves attaching a vibratory hammer to the top of the pile. The hammer produces vertical vibrations that temporarily liquefy the surrounding soil by reducing its effective stress and cohesion, thereby driving the pile to a predetermined depth.

Figure 1.7: Vibratory hammer installation of pile in offshore environment (taken from [24])

1.1.3. Floating foundation and pull-out capacity

Floating offshore wind turbines have emerged as a promising solution for harnessing wind energy in deep-sea environments where traditional fixed-base turbines are not feasible. Compared to fixed foundations, floating platforms offer advantages in deployment, maintenance, and environmental impact [25]. Their installation relies on mooring systems to ensure stability under dynamic ocean conditions, with mooring lines typically anchored to the seabed via piles. As shown in Figure 1.8, the most widely used floating foundations all depend on mooring lines which are connected to the anchor piles embedded in the seabed to maintain stability. These anchor piles are subjected to complex inclined tensile loading, a scenario that significantly differs from the vertical or compressive loading typically considered in pile design. Higher pull-out capacity of these anchor piles will help to improve the safety of floating foundations, as well as save maintenance costs for a long operating time; thus, finding an optimal solution for installing these anchor piles is necessary.

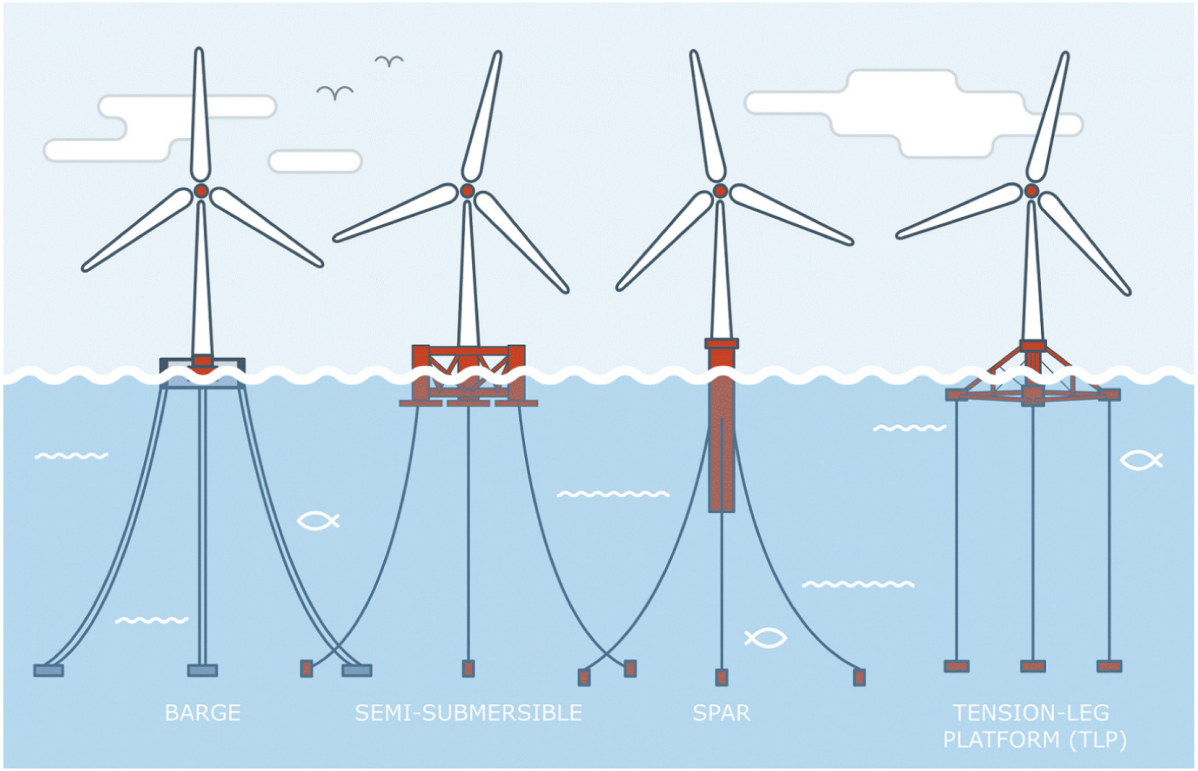

Figure 1.8: Sketches of four types of floating offshore wind turbine foundations (from left to right: barge, semi-submersible, spar, and TLP) (taken from [26])

1.1.4. Problem definition

The different driving methods will induce distinct mechanical behaviors in the surrounding soil, such as soil plugging and stress redistribution. Despite advancements in experimental and numerical studies, the micro-mechanical mechanisms underlying these interactions remain poorly understood, limiting the optimization of installation techniques and structural reliability. This research aims to address these gaps by utilizing Discrete Element Method (DEM) simulations to analyze soil-pile interactions under various installation methods, providing insights to enhance installation efficiency and reduce environmental impact.

2

Numerical Study of Pile Installation

2.1. Motivation for DEM-Based Modelling

Traditional experimental approaches—such as full-scale field tests and centrifuge modeling—have long been employed to investigate pile installation mechanisms. However, these methods are often constrained by high costs, scale effects, and limited observability. As a result, numerical simulations have become increasingly popular in pile research. Among them, the Discrete Element Method (DEM) stands out for its ability to resolve micro-mechanical particle interactions, making it especially suitable for modeling soil-pile interaction during installation and pull-out processes.

Compared to continuum-based methods such as finite difference method (FDM), finite element method (FEM), and boundary element method (BEM), which assume a continuous soil medium, DEM treats soil as an assembly of discrete particles, capturing phenomena like soil arching, plug formation, contact evolution, and dilation directly at the particle scale. A summary comparison is presented in Table 2.1.

Table 2.1: Comparison of numerical methods for pile simulation

Method	Main Advantages	Main Limitations
FDM	Simple formulation; efficient for certain transient problems	Assumes continuum; less accurate for complex geometries
FEM	Relatively low computational cost; commercial tools available	Assumes continuum; mesh distortion in large deformation
BEM	Efficient for infinite domains	Not suited for highly nonlinear media
DEM	Captures particle-scale behavior; suitable for large deformation	High computational cost; calibration needed

2.2. State-of-the-Art DEM Applications in Pile Studies

2.2.1. 2D DEM Simulations

Recent studies have used 2D DEM to analyze key processes such as soil plugging, stress redistribution, and frictional resistance. For instance, Li et al. (2019) developed an arching-based model to explain load transfer in open-ended piles [27], while Duan et al. (2021) identified the effect of dilation and contraction near the pile tip during jacking [28]. Bai et al. (2024) directly compared jacking and impact installation methods using DEM, revealing significant differences in plug evolution and penetration resistance [29].

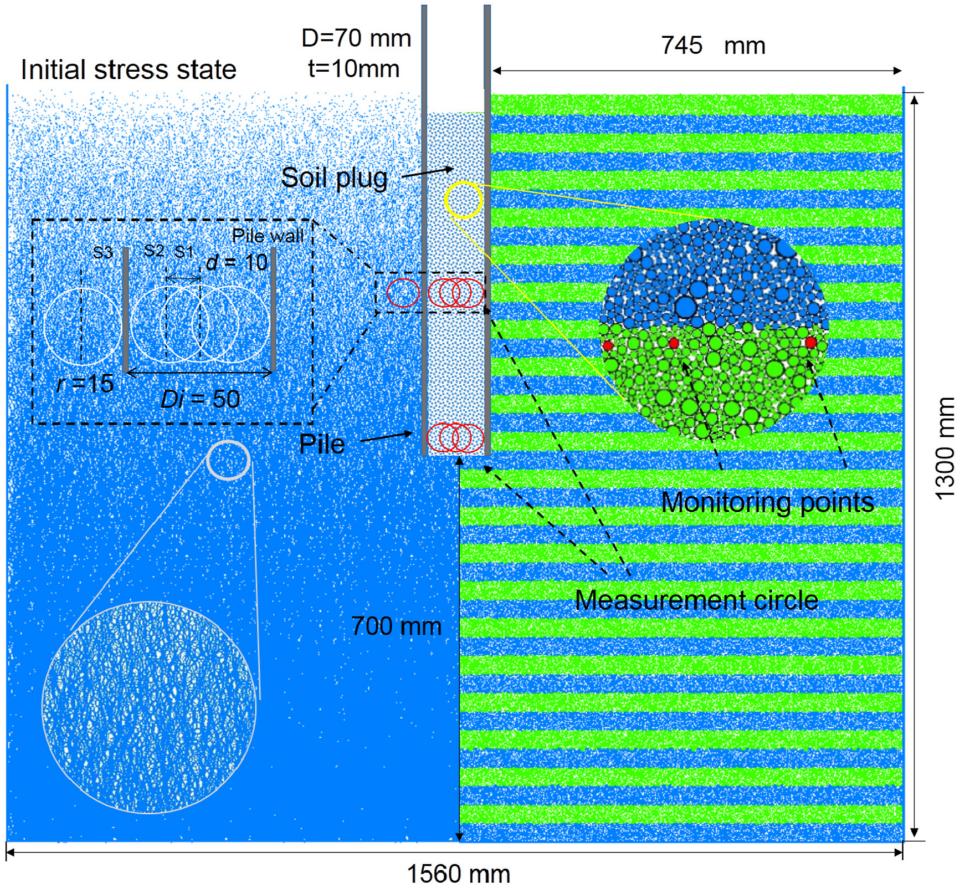

Figure 2.1: DEM model setup for open-ended pile installation [30]

2.2.2. 3D DEM Simulations

With increasing computational power, 3D DEM is now used to obtain more realistic soil responses. Guo et al. (2023) demonstrated stress arching mechanisms around displacement piles [31], and Feng et al. (2024) investigated pile resistance and lateral friction in sand [32]. These studies highlight the capability of 3D DEM in capturing complex spatial interactions during pile penetration.

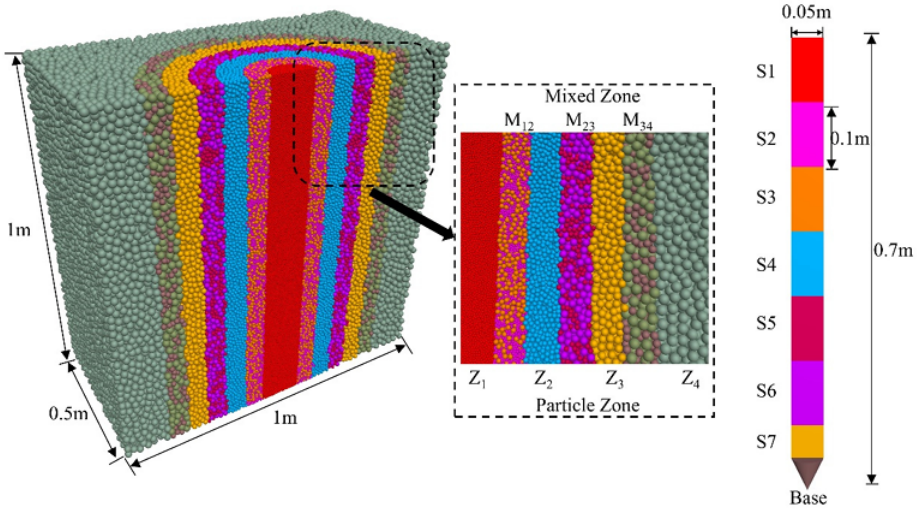

Figure 2.2: 3D DEM model setup example [32]

2.3. DEM Platform: LMGC90 and NSCD Framework

This research employs LMGC90, an open-source platform implementing the Non-Smooth Contact Dynamics (NSCD) method. NSCD enables efficient simulation of rigid-body particle systems with frictional contact and impact, making it highly suitable for large-deformation problems such as pile installation.

Key numerical strategies in LMGC90 include implicit time-stepping, the Nonlinear Gauss-Seidel (NLGS) solver for contact resolution, and OpenMP-based parallelization. These tools enable stable simulation of tens of thousands of particles with a reasonable computational cost.

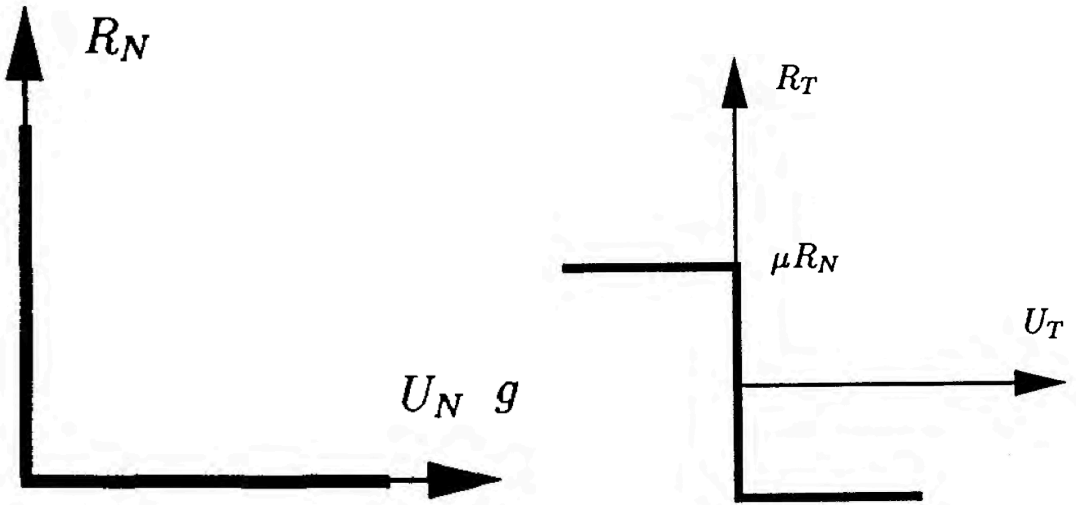

Figure 2.3: NSCD principles: (Left) Signorini condition; (Right) Coulomb friction law [33]

NSCD calculates contact forces by treating them as reaction forces that enforce non-penetration constraints and frictional laws. Unlike soft-contact DEM approaches that model particles with overlaps, NSCD treats particles as rigid bodies, and contact interactions are formulated through a velocity-impulse framework. At each time step, the method determines the contact forces by finding values of the relative velocities and impulses that satisfy both the equations of motion and the contact/friction laws. This is done by treating the contact conditions (no penetration and Coulomb friction) as constraints and adjusting the forces until these constraints are met for all contacts simultaneously. In NSCD, this search is formulated mathematically as a problem where the unknown forces must lie within certain allowable regions (defined by the contact laws), and the solver iterates over all contacts until a consistent set of forces is found. In this framework, the contact force is implicitly derived as a Lagrange multiplier associated with the non-penetration constraint, ensuring that the relative velocity at the contact point satisfies both the Signorini's condition (no interpenetration) and Coulomb's law of friction.

The use of rigid particles and the strict enforcement of non-penetration means that NSCD does not allow particle deformation or interpenetration under loading. While this treatment offers numerical robustness and avoids the need for artificial stiffness tuning, it also introduces several limitations. As Dubois et al. noted [34], the velocity-level formulation of unilateral constraints may result in numerical inter-penetrations due to the explicit evaluation of contact gaps, which could affect accuracy in densely packed configurations. Additionally, the inherent rigid-body assumption leads to global and local indeterminacy in contact force distribution, potentially slowing down the convergence of the nonlinear Gauss-Seidel solver and yielding non-unique contact force solutions [34]. These limitations imply that NSCD may be less suited for dynamic processes where short-lasting momentum transfers between densely packed grains are dominant. In the context of pile installation, such issues may affect the representation of soil densification and the estimation of contact pressures near the pile-soil interface. Nevertheless, the method remains advantageous for simulating bulk kinematics and force transmission in large-scale granular systems such as pile pull out, where the process is purely controlled by the grains and pile frictional contacts.

2.4. Conclusion

DEM provides a powerful framework for simulating pile installation and pull-out, particularly when particle-scale behaviors such as soil plugging and arching are of interest. Combined with a robust computational engine like LMGC90, DEM enables insight into complex interaction mechanisms that are difficult to access through experiments or continuum modeling. This chapter lays the foundation for the DEM simulations presented in the following chapters.

3

Jacking Simulation

In the previous researches using LMGC90, there were only a small number of pile installation simulations, and most of these models were not validated before. Before performing simulations of impact driving and vibratory driving, we decided to start with jacking simulation, which is the simplest pile installation method. After the numerical simulation, the results are further validated by comparing with an existing pile jacking DEM simulation performed by Bai et al. in 2024 [29]. In order to simplify the validation process, the scale of the model, as well as soil and pile properties, is kept the same as Bai et al. used.

3.1. Numerical Modeling

In this part, the process of how we build the model using LMGC90 will be introduced in detail, including parameter decision, model build-up steps, simulation strategy, and numerical parameter calibration.

3.1.1. Parameter Decision

In order to simplify the later validation process by comparing our numerical results with Bai et al., the parameters used in our LMGC90 model should be as close to those used by Bai et al. as possible. Soil and pile parameters used in the LMGC90 model are shown respectively in Table 3.1 and Table 3.2.

Table 3.1: Material properties of soil sample [29]

Properties	Numerical value	Unit
Particle density	1650	$\mathrm{kg/m^3}$
Coefficient of friction	0.1	$-$
Maximum radius	5.5	mm
Minimum radius	4.9	mm
Average radius	5.2	mm

Table 3.2: Pile parameters of numerical simulation [29]

Property	Value	Unit
Length	1	m
Inner diameter	50	mm
Wall thickness	20	mm
Coefficient of friction	0.5	$-$
Normal stiffness	1.5×10^8	$\mathrm{N/m}$
Tangential stiffness	1.0×10^8	$\mathrm{N/m}$
Poisson's ratio	0.2	$-$
Density	2500	$\mathrm{kg/m^3}$

From Table 3.1, it is worth noticing that the coefficient of friction of this soil is small (0.1), which will reduce the shear resistance between particles. As a result, it can be expected that during pile installation, the rearrangement of soil will be significant, leading to unrealistic behavior such as extremely long soil plug formation, a wide range of soil displacement fields, and settlement rather than uplift on the ground surface.

Moreover, when looking into the pile thickness and soil particle size, it can be seen that the diameter of the pile is only 2.5 times the pile thickness, but according to Randolph et al. and Yang et al. [35, 36],the typical pile configuration used in offshore foundations should have at least 25 as the diameter-thickness ratio. Therefore, the model pile in this study is rather small compared to the real situation. In order to save simulation time, the soil particle average radius is 5.2 mm; this is a lot larger than real soil particles. All these scaled model diameters will cause some limitations; for example, larger particle size will lead to a smaller amount of contact between soil and pile, leading to lower shaft friction of the pile. However, even though the parameters of the model are unrealistic compared to the real situation, it is still sufficient for investigating the qualitative trends of pile-soil interaction and capturing certain behaviors during pile installation and extraction.

Even though this model provides observations in a two-dimensional model (2D), the insights from it are expected to be reproducible in a three-dimensional domain (3D). It is expected that greater grain rearrangements would lead to more uniform displacement fields around the pile. Future research should aim to look closer at this equivalency and confirm if the lower computational cost of a 2D model compensates for that of a 3D system.

Additionally, the scale of the soil container, which represents the size of the domain, is 2.5 m in width and 1.25 m in depth. This is a closed box, and the four walls (left, right, bottom, and top) are all smooth walls, which means that the coefficient of friction is 0. LMGC90 uses several rectangular elements to assemble a smooth wall; in our study, each wall contains 12 rectangles. The thickness of each wall is set as 5 times the maximum soil particle diameter, and the length of each wall is 10 meters in order to avoid particles from running out of the domain.

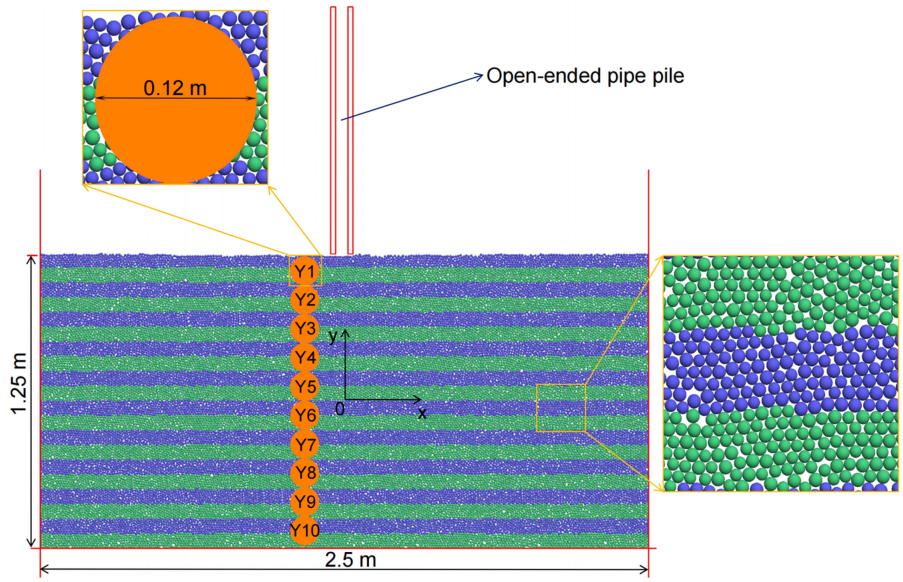

Figure 3.1: Pile installation model to be validated [29]

As LMGC90 does not support the direct creation of complex rigid body geometries, the open-ended pile was constructed using a mesh-based approach. Initially, the eight vertices defining the pile's geometry were specified in a clockwise sequence, and the enclosed region was subsequently meshed using Gmsh with a mesh size of 0.01 m and a mesh shape of triangle. This mesh was imported into LMGC90 to define a rigid avatar, which was then precisely positioned at the center of the domain to represent the open-ended pile used in this simulation.

3.1.2. Simulation Campaign

Model generation and compaction

The main goal of this stage is to create the open-ended pile, soil particles, and soil container, as well as performing the ”pre-compress” process mentioned by Bai et al. This aims to make the specimen distribution more uniform, in order to better simulate the real construction situation.

First of all, a list of particle radii is created by using random numbers varying from a minimum radius (4.9 mm) to a maximum radius (5.4 mm), which were used by Bai et al. in 2024 [29]. After that, the centers of these particles are automatically determined using the function ”depositInBox2D” provided by LMGC90. In this function, dense deposit of particles is performed by minimizing the total potential [37]. Further, random radii and material properties are given to these generated centers to create soil particles. In the study of Bai et al., coastal silty soft soil is used, and the material properties applied to the numerical model are shown previously in chapter 3 Table 3.1.

Secondly, four rough walls are generated to hold the soil sample. The rough wall in LMGC90 is made of a cluster of disks. In order to make the system easier, the rough walls use the same material as the open-ended pile (concrete). The walls are made 1.2 times longer than the width and height of the deposit area in order to make sure that all soil particles can be held in the box. As a preparation for further pre-compression procedure, the degrees of freedom in the horizontal and vertical directions are set as ’force’ controlled for the vertical and horizontal walls, respectively. The values equal to the vertical stress induced by the self-weight of the soil sample at the base of the box, which is $\rho g h$, in which ρ is the particle density, g is gravity acceleration, and h is the height of the soil sample. One thing worth noticing is that for these walls the geostatic stress is converted into force by normalizing it by an equivalent area of 1 m^2.

Finally, the model pile should be created at the middle top of the area for further simulation. Due to the concave polygon shape of the pile, it is created using a 2D mesh rather than a combination of polygons. Gmsh is an open-source finite element mesh generator [38]; the pile is divided into a 2D mesh using this software, and then the mesh file is read by LMGC90 to generate the pile body. Material parameters of concrete are given to the pile, and the pile properties are shown in table 3.2. Also, the pile is fixed in all three degrees of freedom. The boundary conditions introduced are shown in Figure 3.2.

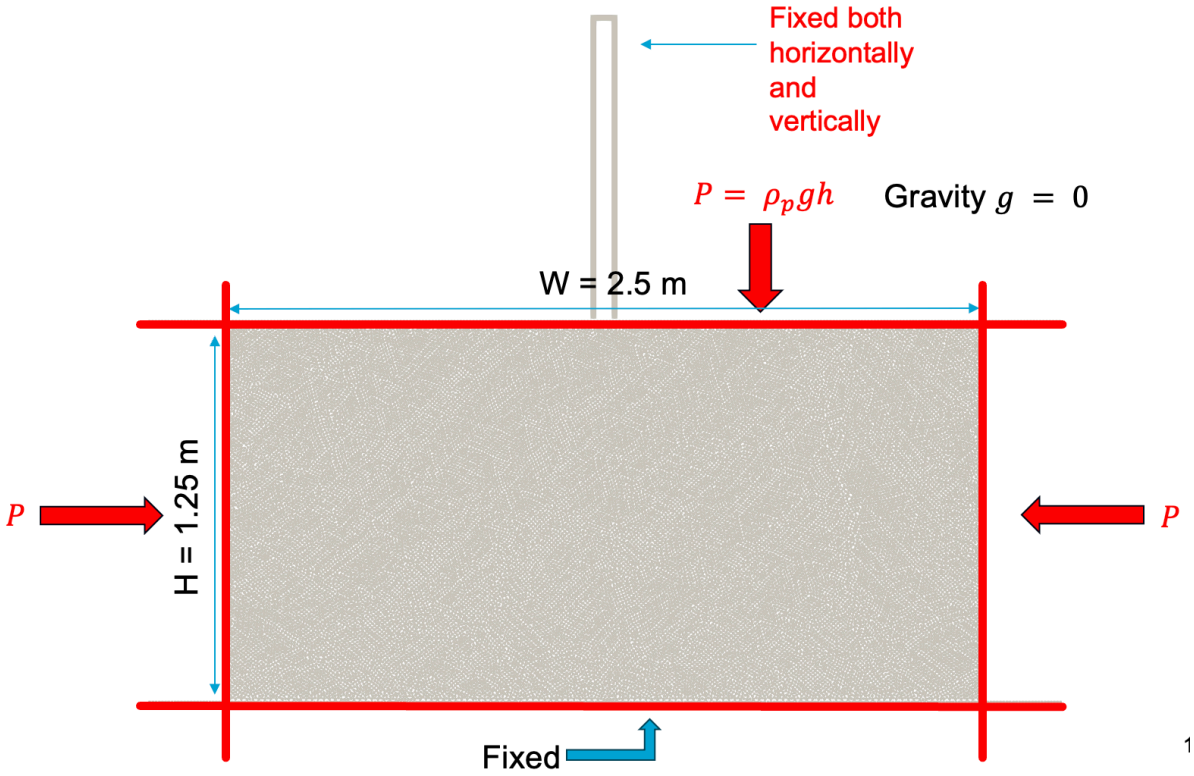

Figure 3.2: Boundary conditions for compaction stage

Particle stabilization

In the previous stage, the soil sample was compacted to a dense state. However, due to the external force applied to the soil sample, the stress state inside the sample is unrealistic, and after compaction, the soil particles still have residual kinetic energy, which means that the whole system is far from the natural situation. In order to simulate the state that is closest to the natural situation, we have to ensure a realistic geostatic stress state and mechanical equilibrium of the whole soil sample. To achieve this, the soil sample has to be stabilized under gravity after the pre-compaction process.

In this stage, the left, right, and bottom walls are kept fixed, while the top wall is removed from the model. The gravity field is activated in order to let soil particles move under the influence of their self-weight. The pile is fixed both horizontally and vertically, which means that in this stage, the pile still has no contact with the soil sample. The boundary conditions used in this stage are shown in Figure 3.3.

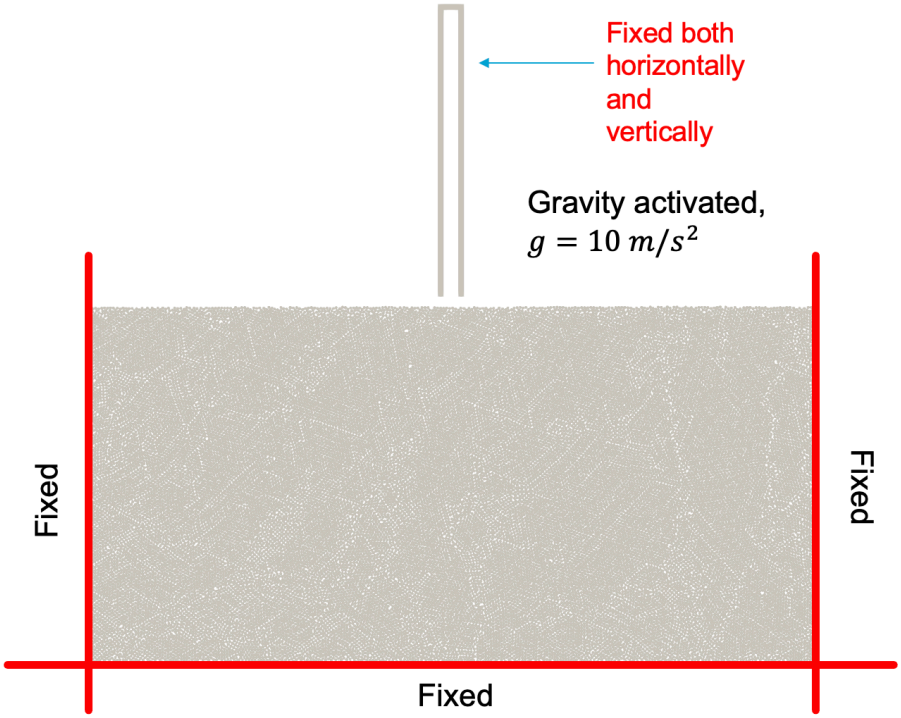

Figure 3.3: Boundary conditions for stabilization stage

Pile self-weight penetration

Since the soil body has reached the expected state, the pile can be installed into the soil. Before driving the pile into the soil, the pile is supposed to be put in the expected location and penetrate into the soil by its self-weight.

In this stage, the three walls used as the box are still fixed, while the gravity field is kept activated. However, in this stage, the pile is free to move vertically under its self-weight, but it is still fixed horizontally. The boundary conditions for the self-weight penetration stage are shown in Figure 3.4.

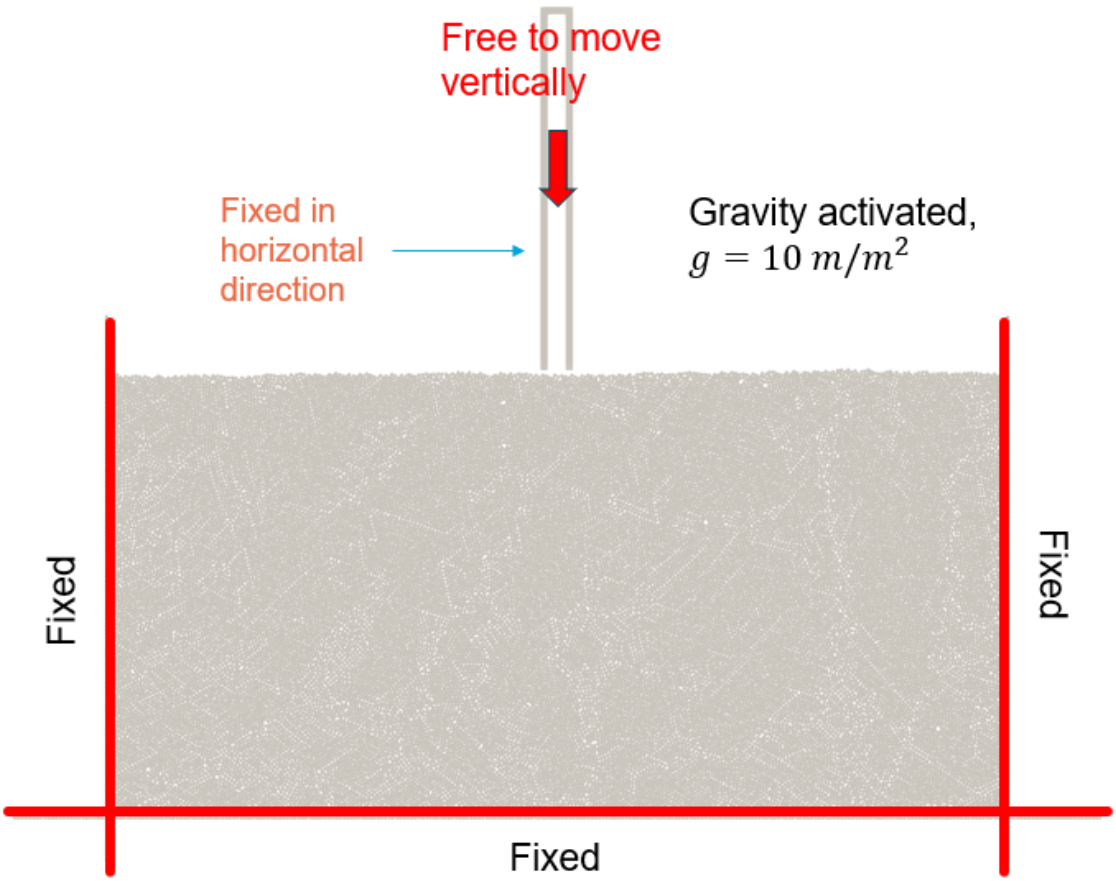

Figure 3.4: Boundary conditions for self-weight penetration stage

Pile jacking

For pile jacking simulation, the second driven degree of freedom of the pile is changed from force to velocity, which is set at a constant velocity of 0.02 m/s. The whole jacking process takes 40 seconds in total until the entire pile is penetrated into the soil.

In this stage, the three walls of the box are still fixed, and the gravity field is kept activated. Meanwhile, the pile is given a constant velocity of $-0.02m/s$, in which the negative value stands for downwards. The boundary conditions used in this stage are shown in Figure 3.5.

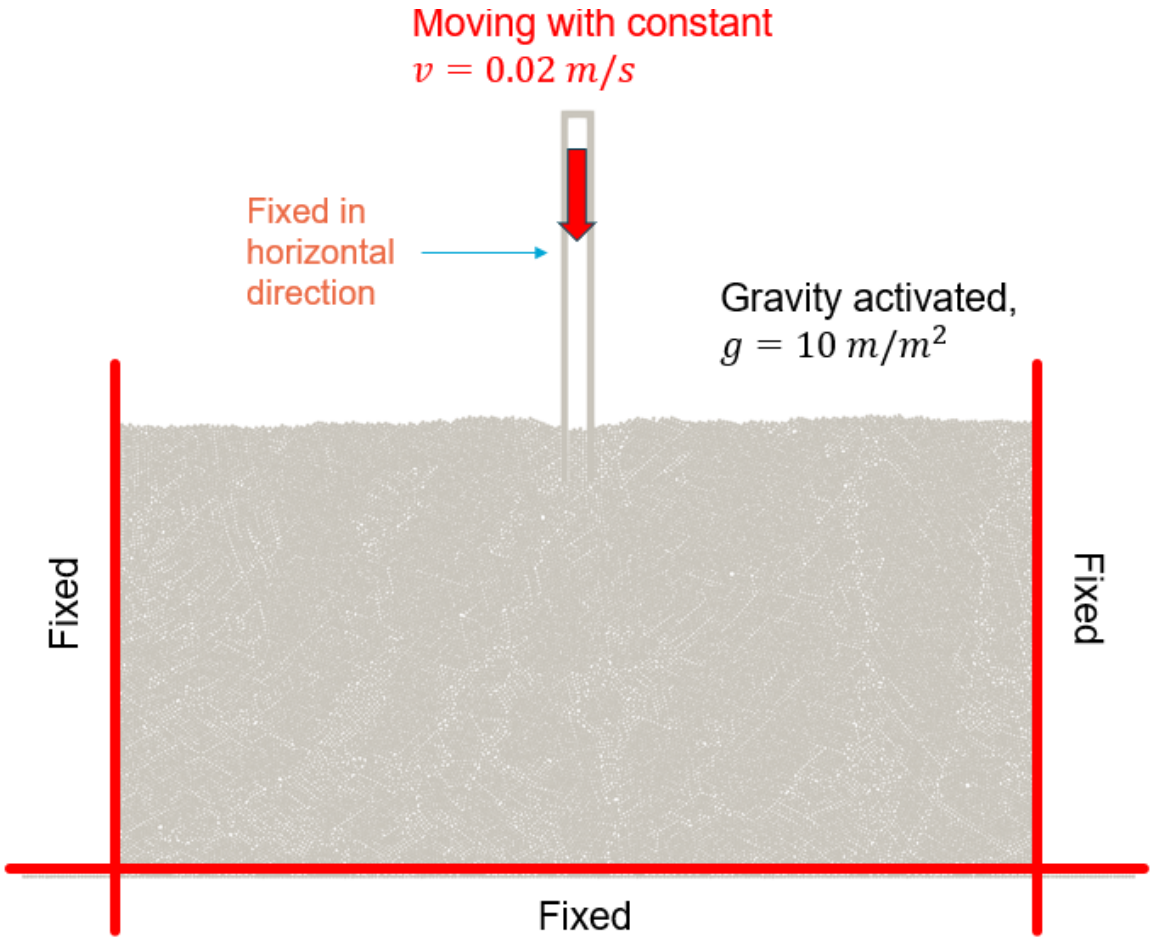

Figure 3.5: Boundary conditions for jacking stage

In the jacking simulation, the time step Δt is determined based on the dynamic stability criterion equation 3.4. In this jacking simulation case, ρ_p is the particle density $1650kg/m^3$, $r_{\min}$ is the smallest particle radius $0.0049m$, and h is the height of the soil layer $1.25m$.

Considering the jacking process, the pile penetration velocity is relatively low ($v = 0.02$ m/s), which means that the interaction among rigid bodies is slow. According to the penetration length, the total penetration time T can be estimated as:

$$T = \frac{L}{v} = \frac{0.8\ \text{m}}{0.02\ \text{m/s}} = 40\ \text{s} \tag{3.1}$$

Given the low driving velocity and the relatively long total simulation time, the safety factor can be relaxed to $1/50$ without significantly affecting numerical stability. Therefore, the adjusted time step Δt becomes:

$$\Delta t = \frac{1}{50}\left(\frac{\rho_p \cdot (2r_{\min})^2}{\rho_p g h}\right)^{1/2} \tag{3.2}$$

Using the specific values from the current setup, the final time step adopted for the jacking simulation is approximately:

$$\Delta t \approx 5.54 \times 10^{-4}\ \text{s} \tag{3.3}$$

3.1.3. Time step

In Discrete Element Method (DEM) simulations, the selection of a suitable time step Δt is critical to guarantee both numerical stability and accuracy. In classical molecular dynamics (MD) based DEM

software, such as PFC2D, the time step is often determined using the Rayleigh wave propagation, which represents the time for elastic waves to propagate from one particle to the adjacent contacting particles. [39, 40]. This is a good estimation because the difference between the Rayleigh and distortion wave velocities is very small, and the energy transferred by the expansion wave is negligible [41]. Furthermore, the average time it takes for a Rayleigh wave to reach any contact point is the same, regardless of the location of the contact point.

However, in the Non-Smooth Contact Dynamics (NSCD) framework adopted by LMGC90, the situation differs significantly. Unlike MD-based DEM, in which a small amount of overlapping is allowed to happen during contact among particles, NSCD imposes non-penetration constraints through an implicit, time-discrete resolution of velocity and force constraints. Consequently, the time step is no longer governed by contact stiffness, but rather by the propagation of momentum and the resolution of impulsive forces [42].

Despite this, to maintain a stable iterative convergence of the contact solver (e.g., the Gauss-Seidel type fixed-point method used in LMGC90), a time step that is too large may hinder the detection and resolution of contacts within a short period of time, or induce artificial overlap due to numerical drift. Therefore, in practice, even within the NSCD framework, a pseudo-physical criterion is used to estimate a conservative time step.

In our simulations, we adopt an empirical formulation based on the characteristic stress induced by gravity, and minimum particle radius, as previously suggested in the literature for quasi-static problems involving gravity-dominated loading [42]:

$$\Delta t = \frac{1}{100}\left(\frac{\rho_p \cdot (2r_{\min})^2}{\rho_p g h}\right)^{1/2} \tag{3.4}$$

Here, ρ_p denotes the particle density, $r_{\min}$ is the smallest particle radius in the sample, and $\rho_p g h$ represents the gravitational stress at the bottom of the soil layer, with h being the height of the sample. The coefficient $1/100$ is a safety factor introduced to reduce solver instability, particularly under highly packed conditions or during dynamic events such as compaction or penetration. Since this formula is based on empirical insights, it serves as a practical guideline rather than a strict requirement. In practice, the factor in equation 3.4 can be adjusted based on the total number of particles. For example, in our reproduction involving 30,302 particles, a relaxed factor of 1/50 was employed to accelerate the simulation while maintaining numerical stability.

This formulation has proven effective in ensuring the convergence of the contact solver while maintaining the physical realism of the simulated response, especially in large-scale granular assemblies under quasi-static loading.

The time step values used in each simulation step are shown in Table 3.3.

Simulation step	**Time step value**
Compaction	$5.54 \times 10^{-5} s$
Particle stabilization	$2.77 \times 10^{-4} s$
Pile self-weight penetration	$5.54 \times 10^{-5} s$
Pile jacking	$4.90 \times 10^{-4} s$

Table 3.3: Time step settings for each simulation stage

3.1.4. Numerical parameters

To solve the friction-based contact problem between particles and structural boundaries, the Non-Smooth Contact Dynamics (NSCD) approach is adopted in LMGC90. This method handles contact and friction through the use of set-valued force laws and time-stepping schemes that allow for the enforcement of unilateral constraints without regularization [43, 44].

The temporal discretization is performed using a θ-method with $\theta = 0.5$, corresponding to the mid-point rule. This semi-implicit scheme is unconditionally stable in the linear regime, and it offers good energy conservation properties in large-deformation dynamic systems [33].

The iterative contact solver used in this study is based on the Gauss-Seidel-like approach, which iteratively solves the contact problem at each time step. The following numerical settings are adopted:

- **Contact resolution type:** `Stored_Delassus_Loops`, which accelerates convergence by storing and reusing the Delassus operator over iterations, reducing the computational cost in systems with repeated contact configurations [45].
- **Norm:** `QM/16`, referring to a quadratic minimization-based norm with 16 sub-partitions used to evaluate the convergence of residuals during iterations. This norm offers a balanced trade-off between convergence accuracy and computational overhead.
- **Tolerance:** $\texttt{tol} = 10^{-5}$, which sets the convergence threshold for the iterative solver. Once the residual norm falls below this value, the system is considered converged for the current time step.
- **Relaxation factor:** $\texttt{relax} = 1.0$, indicating that no under-relaxation is applied. In some highly nonlinear problems, relaxation factors below 1.0 can be used to dampen oscillations, but in this quasi-static scenario, full relaxation was sufficient.
- **Iteration limits:** $\texttt{gs\_it1} = \texttt{gs\_it2} = 100$, representing the minimum and maximum number of Gauss-Seidel iterations per time step. Setting both limits to the same value ensures that each step is solved to a uniform convergence standard, which is especially important in high-contact-density systems such as soil compaction and pile penetration.

These parameters were selected based on best practices in NSCD simulations for granular media and contact-dominated problems [46, 47]. They ensure robust and consistent convergence in the presence of numerous simultaneous frictional contacts, as commonly encountered in dense particle assemblies.

3.2. Results

3.2.1. Model generation and compaction

In this pre-compression stage, the main property that needs to be noticed is the change of density of the soil sample during this process. This can be determined using the change in displacement before and after the pre-compaction process. The differential contour map is shown in Figure 3.6. In the contour map, the displacement is normalized by dividing it by the mean particle diameter (0.0052 mm).

From the contour map, it is clear that after the pre-compaction process, most of the soil particles experience a large amount of displacement, which means that this process compacted the soil sample and increased the density of the sample significantly.

3.2.2. Particle stabilization

During the pre-compaction process, the horizontal and vertical movement of the left, right, bottom, and top walls was traced respectively. The coordinates' evolution over time plots for the four walls are shown in Figure 3.7. From the figure, three pink dashed lines can be seen in the plots; this means the time points at which the walls stop moving, meaning that the soil sample reaches its densest state. Further, the blue 'X' symbols show the final time step of the pre-compaction simulation process. The period from the pink dashed line to the blue 'X' will be used as the particle stabilization duration.

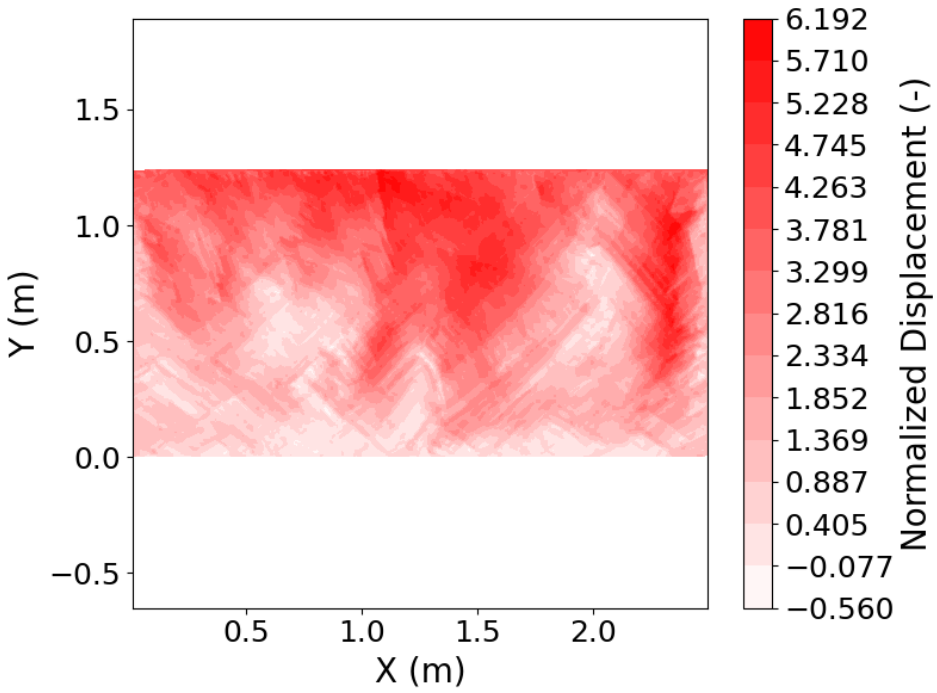

Figure 3.6: Difference in displacement before and after pre-compaction (positive value means moving upward, negative means downward)

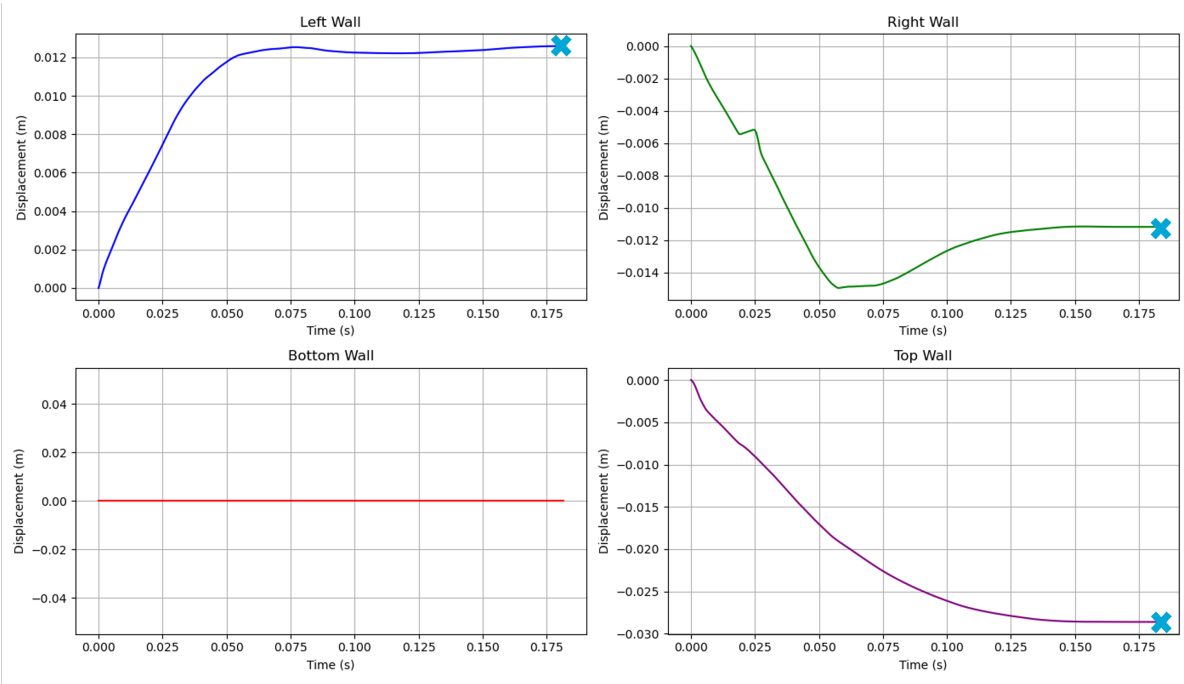

Figure 3.7: Coordinate changes over time for four walls (final state labeled by blue cross)

In the simulation, first, the top cap of the box is removed to prepare for pile penetration. After that, the geometry, material, and driven degree of freedom properties of the whole system are kept the same as the previous stage to let the soil particles stabilize under their self-weight. After the duration period mentioned before, the displacement of all particles becomes 0; stabilization is recognized as having been reached, and this step comes to an end.

3.2.3. Pile self-weight penetration

In this stage, a criterion for judging whether the self-weight penetration of the pile has ended is used in the simulation. This criterion is that when the vertical displacement of the pile is less than 0.1 mm in one hundred time steps, we consider that the self-weight penetration of the pile has ended. In Figure 3.8, the progress of self-weight penetration depth L/D, which is the ratio between pile penetration depth and diameter of the pile, competing with time is shown. In the plot, the time when the self-weight penetration stage stops is labeled as a blue cross, which is around 0.5 seconds after the start of this stage. The total amount of L/D is about 4.5, which means that the pile moves around 4.5 times its diameter under the influence of gravity.

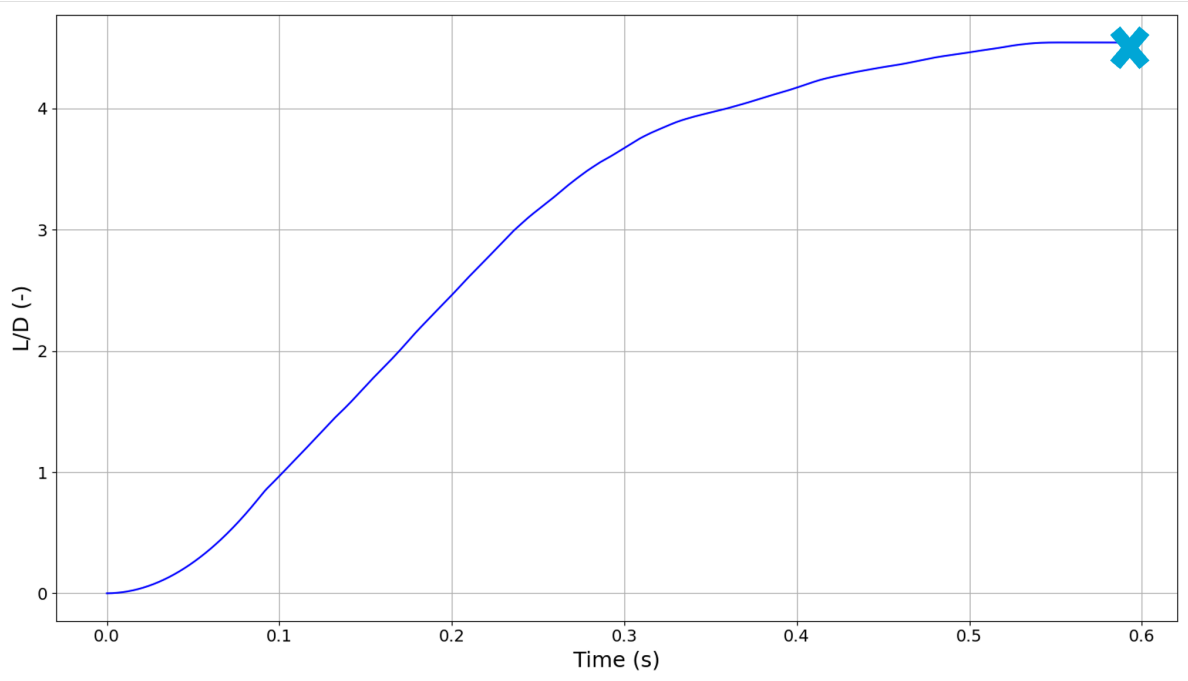

Figure 3.8: Self-weight penetration depth evolution with L/D (final state labeled by blue cross)

3.2.4. Pile jacking

The final state after jacking simulation is shown in Figure 3.9. From the screenshot, it can be seen that the soil exhibits evident localized deformation around the pile shaft, while the far-field soil structure remains largely undisturbed. The soil on both sides of the pile is lifted, indicating particle rearrangement and the formation of shear bands around the pile shaft. Moreover, soil plug appears in the pile body as expected, providing extra inner friction force to the pile.

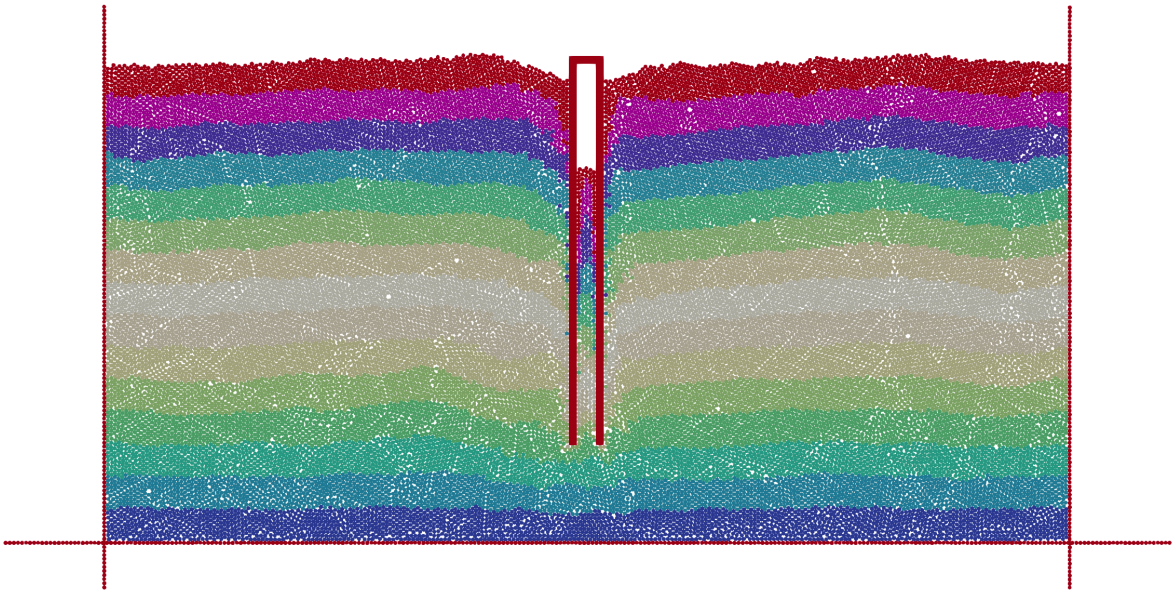

Figure 3.9: Final state after jacking (different grain color represents different layer)

3.3. Numerical Validation

In order to validate our results, a series of comparisons between our numerical results and results obtained by Bai et al. is necessary.

3.3.1. Penetration resistance

First of all, the penetration resistance of the pile needs to be compared. Due to the noisy nature of raw reaction force data obtained, moving average method [48] is applied to smooth the data. The results from this research and Bai et al. are shown respectively in Figure 3.10(a) and Figure 3.10(b).

Because during the model generation process, we created the open-ended pile as a rigid avatar, which means that the pile is considered as a whole, the properties such as forces will be recorded in the center of mass, so that its horizontal and vertical reaction forces are recorded and are available for post-processing, in which the vertical reaction force is the ”total penetration resistance” in research from Bai et al.. From Figure 3.10(a), it can be seen that the reaction force shows large fluctuations while keeping increasing from 0 to around $10000N$. In Figure 3.10(b), the green curve (total penetration resistance) can increase from 0 to around $9000N$. Comparing the increasing trend, fluctuation behavior, and final penetration resistance value, for all these properties, it can be concluded that our simulation results are pretty close to those obtained from Bai et al. [29].

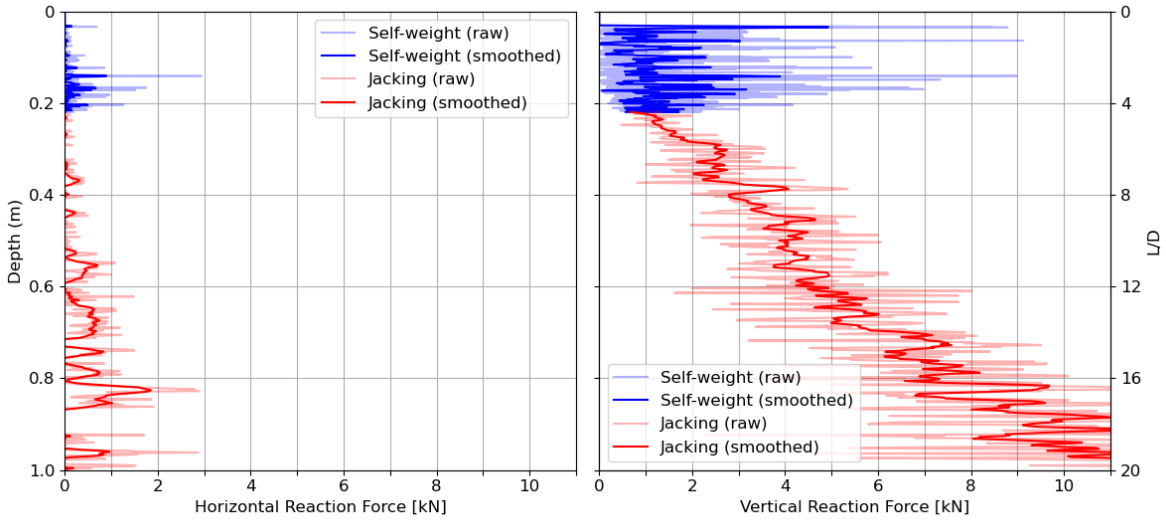

(a) Lateral and vertical reaction force of the pile in this research

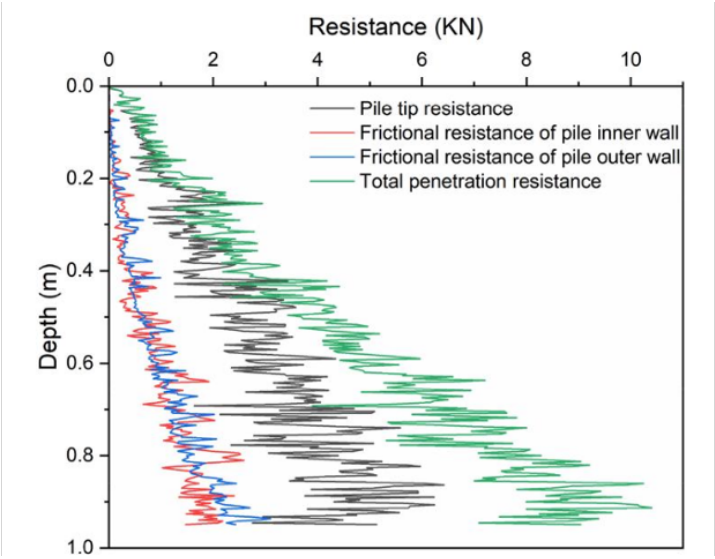

(b) Penetration resistance obtained by Bai et al. [29]

Figure 3.10: Comparison of pile penetration resistance between two studies.

3.3.2. Soil behavior

In research from Bai et al., four states during penetration were recorded, which were respectively when the pile was penetrated $1/4$, $1/2$, $3/4$, and $4/4$ times the pile length into the soil. In this study, these four states are also captured and compared with results from Bai et al. [29]. The comparisons are shown below.

During the pile penetration process, the soil uplifting behavior can be witnessed as soon as the pile starts penetrating into the soil. This is because the pile occupies the volume inside the soil body, which leads to the soil particles moving upwards. In Figure 3.11, the uplifted soil can be observed on both sides of the pile during jacking. In research from Bai et al., it was reported that when the pile penetrated $1/2L$ into the soil, the uplifting became more serious; this is also the case in our research. Moreover, the same clipping area caused by pile shaft friction is also observed. The compression boundary, which is formed due to the base resistance of the pile, appears in our simulation as well. Furthermore, it is clear that with the pile penetrating deeper into the soil, the soil plug within the pile body grows longer, which matches with the behavior in research from Bai et al..

Therefore, our simulation approach resembles qualitatively the simulation results observed in Bai

et al.. The following analyses focuses on comparing micro-mechanical behavior during pile installation, including the displacement field for soil particles, and force evolution along the pile and under the pile tip.

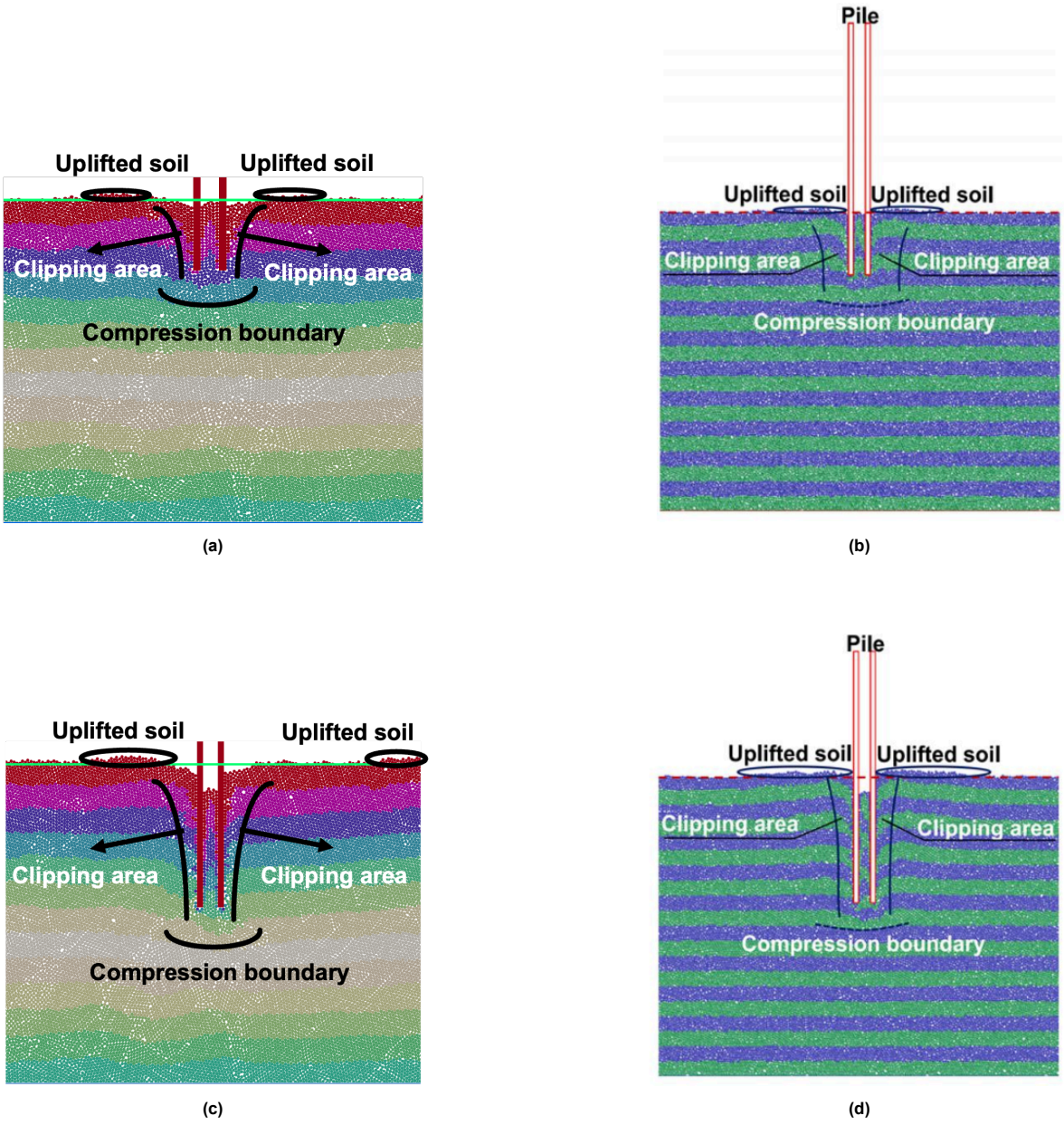

Figure 3.11: First two states during pile jacking process (green line represents soil surface level before self-weight penetration): (a) 1/4 pile length (L) penetration depth from this research; (b) 1/4 L penetration depth from Bai et al.; (c) 2/4 L penetration depth from this research; (d) 2/4 L penetration depth from Bai et al. [29]

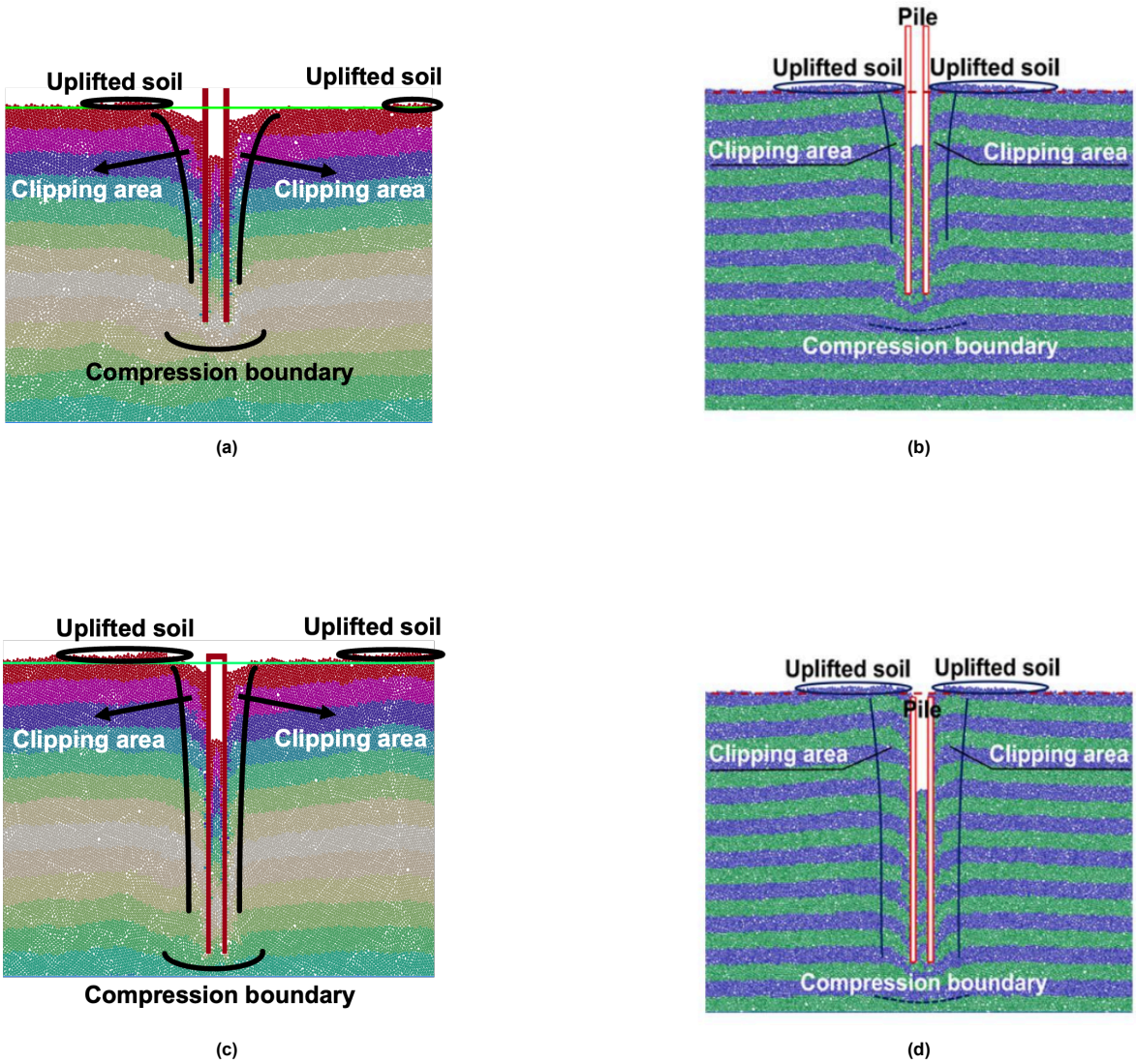

Figure 3.12: Last two states during pile jacking process (green line represents soil surface level before self-weight penetration): (a) 3/4 pile length (L) penetration depth from this research; (b) 3/4 L penetration depth from Bai et al.; (c) 4/4 L penetration depth from this research; (d) 4/4 L penetration depth from Bai et al. [29]

3.3.3. Displacement field

During pile jacking, the displacement field of soil around the pile is also worth detecting. The comparison between the soil displacement field obtained from this research (sub-figures (b) and (d)) and results in the work of Bai et al. (sub-figure (a) and (c)) is shown above in Figure 3.13 and Figure 3.14. From the plots, it can be observed that the magnitudes of displacement are similar; both have the same range. However, in the results from Bai et al., the displacement field near the pile shows a perfectly symmetric cone shape, while in our research the displacement field is asymmetric. For this behavior, it may be caused by the difference in particle radius. In the research of Bai et al., the cone shape shows smooth boundaries between different values, while in our research the boundaries are much rougher, so it can be considered that Bai et al. used smaller particles in their research.

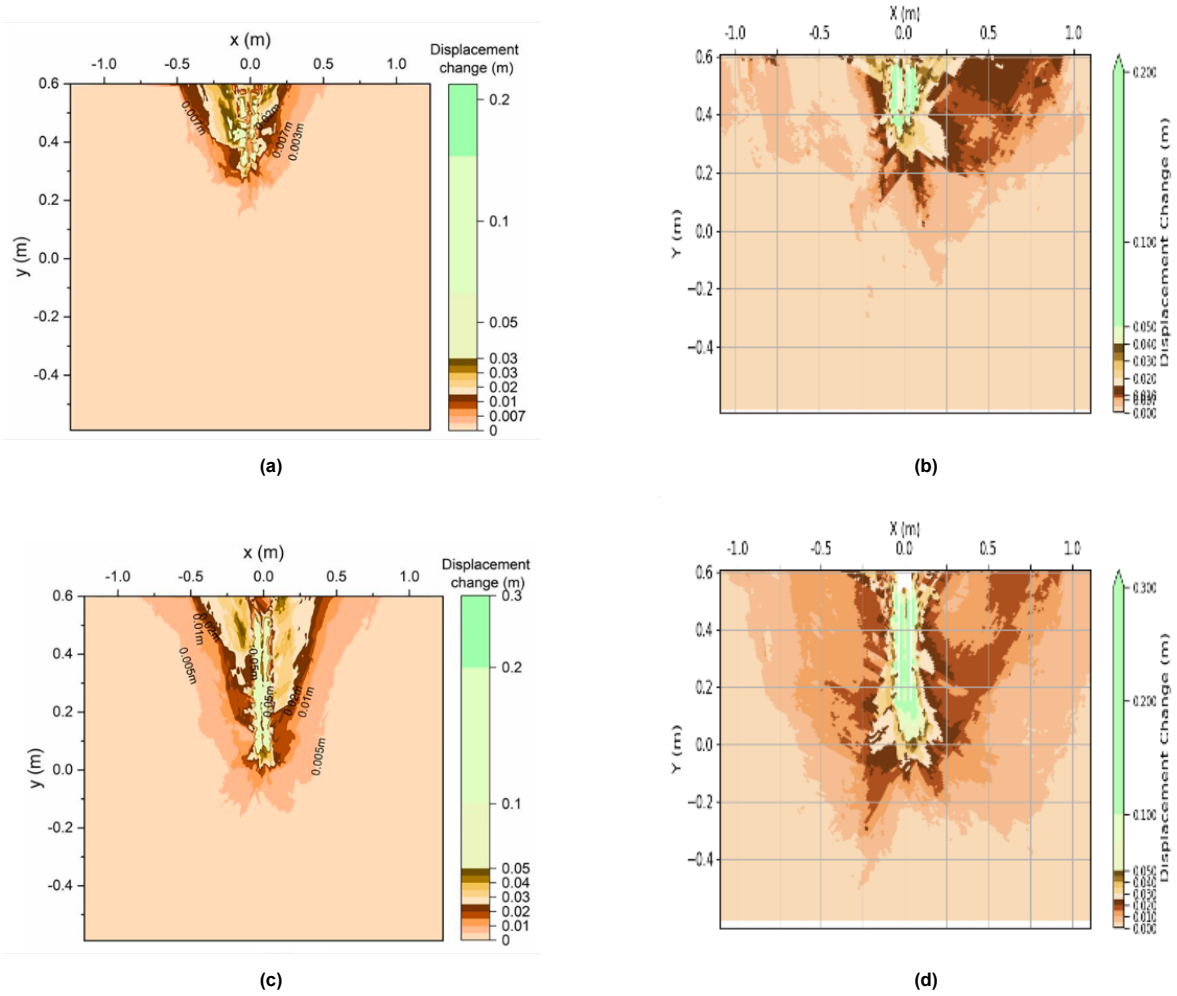

Figure 3.13: Comparison of displacement fields at penetration depth of $0.25L$ and $0.5L$ [29]

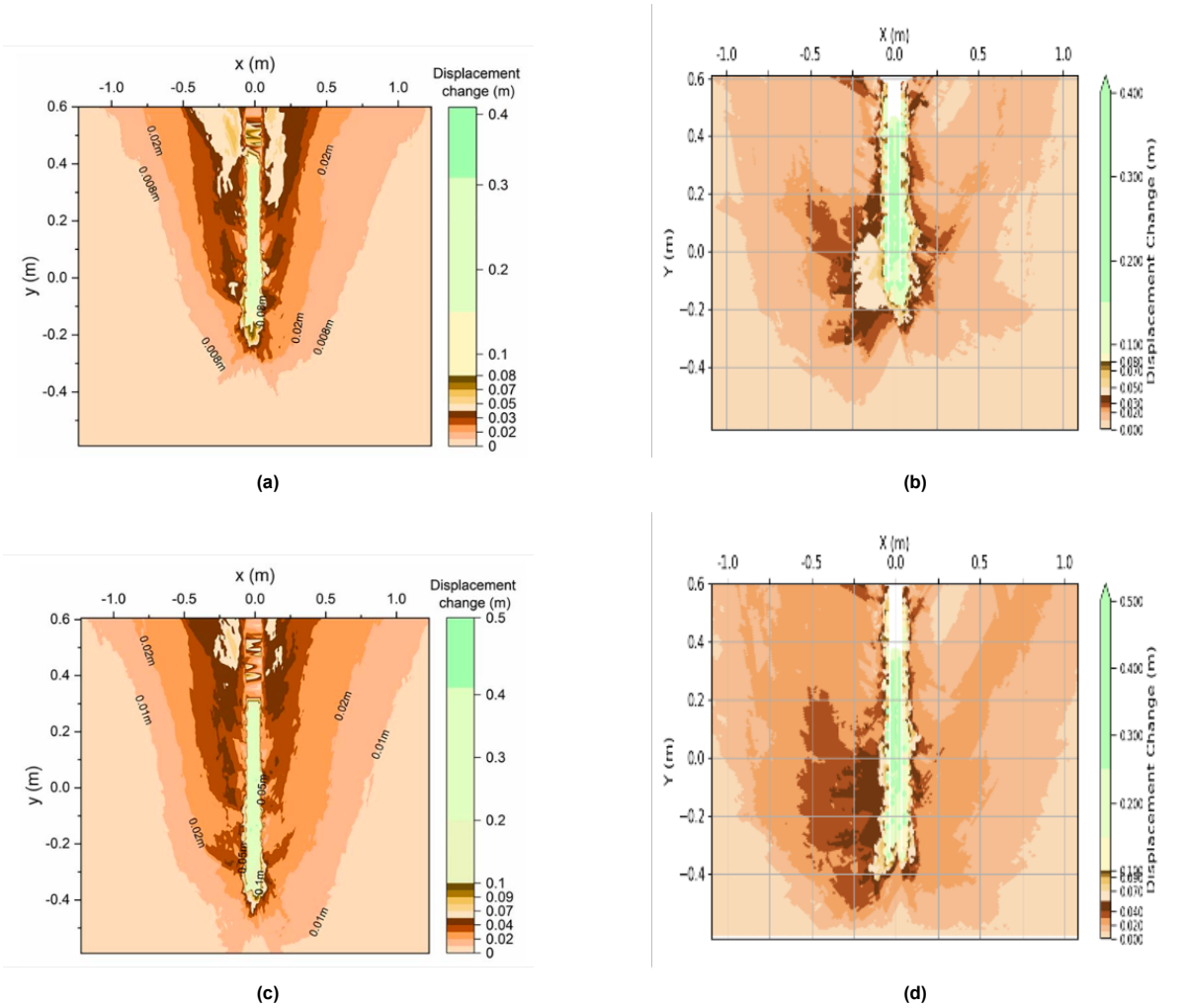

Figure 3.14: Comparison of displacement fields at penetration depth of $0.75L$ and L [29]

3.4. Conclusion

In this chapter, a detailed simulation campaign was conducted to investigate the jacking installation process of an open-ended pile using the LMGC90 software. The model setup, including the generation of soil particles, compaction procedures, pile geometry construction, and simulation boundary conditions, was carefully designed to replicate the conditions reported in Bai et al. (2024), thereby ensuring a consistent basis for validation.

The simulation was divided into four sequential stages: compaction, particle stabilization, pile self-weight penetration, and pile jacking. At each stage, appropriate mechanical and numerical parameters were selected to ensure stability, accuracy, and computational efficiency. The evolution of packing fraction during pre-compaction demonstrated the model's ability to represent realistic soil densification behavior. The self-weight penetration of the pile led to an initial embedment of approximately 4.5D, providing a credible initial state for subsequent jacking.

Validation of the simulation results against the study by Bai et al. confirmed the reliability of our numerical model. The comparison of penetration resistance curves revealed a similar magnitude and trend, while qualitative analyses of soil deformation and displacement fields showed good agreement with published results. Observed phenomena such as soil uplifting, shear band formation, and plug development were consistently reproduced.

Overall, the simulation successfully captured the micro-mechanical behavior of soil during pile jacking and verified the robustness of the modeling framework. This provides a reliable numerical model which can be used for investigations of impact and vibratory driving in the next chapter.

4

Installation Methods Comparison

In chapter 4, the previous model of Bai et al. has been validated. In this part of the thesis, we are about to use the validated model to perform numerical simulations of three different pile installation methods, impact driving and vibratory driving with two different frequencies, to check the influence of pile penetration resistance, as well as the influence of soil around the pile during the installation process. The displacement evolution over time curves for each installation method are shown in Figure 4.1. The method used in this simulation to represent installation methods is velocity control. From the plot, it is clear that the characteristics for each method are different, representing the nature of each method. The simulations for these three methods are performed right after self-weight penetration, which means that the same model after this process is used for all the simulations in this chapter. Moreover, after pile installation, the pile should be removed by pulling, which is also interesting to research. In this part, three installed piles will be pulled out in the same way, and the pulling capacity of them will be analyzed.

4.1. Impact Driving Simulation

Impact driving is one of the most commonly used techniques for pile installation, particularly in offshore and onshore foundation engineering [49]. This method involves striking the pile head repeatedly with a hammer (either hydraulic, diesel, or drop hammer) to break soil resistance and drive the pile into the soil layer. The energy transferred during each blow induces transient stress waves that propagate along the pile, enabling penetration through various soil layers. Impact driving is widely used due to its simplicity, cost-effectiveness, and ability to achieve high penetration resistance in dense soils or soils with variable stratigraphy [50]. Numerical simulation of impact driving can be used to investigate soil-pile interaction during installation, thus providing a better understanding of the nature of this method, such as penetration resistance, soil reaction, and deformation.

4.1.1. Simulation campaign

First of all, the impact driving pile installation method is used to investigate the influence of installation methods. The initial state before installing the pile is used as after self-weight penetration in the previous validation process.

As for boundary conditions, the left, right, and bottom walls are fixed, gravity is activated, and the pile is given a changing velocity to represent the impact driving process. In this stage, the pile is also penetrated into the soil 1 m in depth (pile length), which is the same as the jacking simulation. For simplicity and efficiency of simulation, the whole impact driving process is divided into 10 blows, each blow continuing for 5 seconds. In one blow, the process is divided into three stages: downward moving, bouncing back, and constant.

The downward moving stage represents the hammering process, in which the pile is penetrating into the soil with a constant velocity $0.2m/s$. Considering that the hammering period is quite short (0.6 seconds), it is reasonable that we use constant velocity to represent the movement of the pile in this stage. After hammering is the bouncing back procedure; in this stage, the pile is bounced back due to the elastic deformation caused by hammering. For simplicity and due to the short period of the bouncing

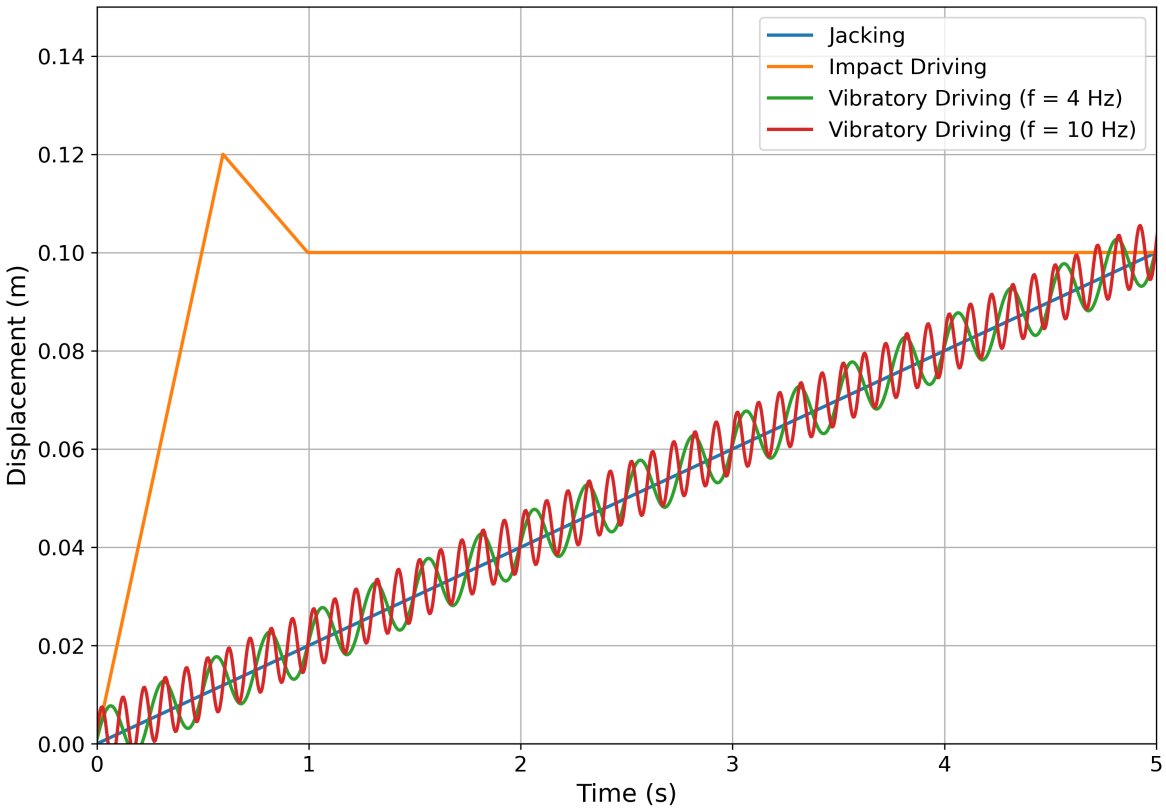

Figure 4.1: Displacement vs time plot for each installation method

back process, the bouncing back velocity is also assumed as constant ($0.05m/s$) and the total time of this procedure is 0.4 seconds. After one blow in impact driving (one hammering + one bouncing back), the pile is kept uninfluenced for a period of time in order to represent the lifting up and falling down process of the hammer. In this research, this period of time is set as 4 seconds.

Table 4.1: Impact Driving Properties

Phases	Time	Velocity
Hammering	0.4 s	0.2 m/s
Bouncing back	0.4 s	0.05 m/s
Constant	4 s	0 m/s

4.1.2. Simulation results

The four states of the system after impact driving installation of 1/4 L, 1/2 L, 3/4 L and L are drawn to be compared with jacking simulation results. The figure of the final state after pile installation for both jacking and impact driving is shown in Figure 4.2. For comparison, similarities and differences between these two methods, one state is enough. From the figure, it is clear that the clipping area, uplifted soil, and compression boundary which are observed in the jacking simulation can also be observed here. Comparing the soil particle distribution during jacking and impact driving processes, no significant difference can be observed. For impact driving installation, the clipping area is shorter and the compression boundary is located deeper than jacking.

The longer clipping area observed in jacking arises from the nature of the loading. In jacking, the pile penetrates the soil at a low, constant velocity, which allows the frictional interaction between the pile shaft and surrounding soil to develop fully over time. This prolonged contact promotes sustained shear deformation along the shaft, resulting in a broader and more continuous shear zone. In contrast, impact driving involves rapid, high-energy blows, where the interaction time between the pile and soil

is fast, leading to more localized and transient shearing.

As for the deeper compression boundary observed in impact driving, due to the high velocity, transient loading applied during impact, stress waves propagate rapidly through the soil mass, mobilizing resistance over a broader and deeper region. This wave-induced energy penetrates further than the quasi-static jacking process, resulting in a deeper compression boundary.

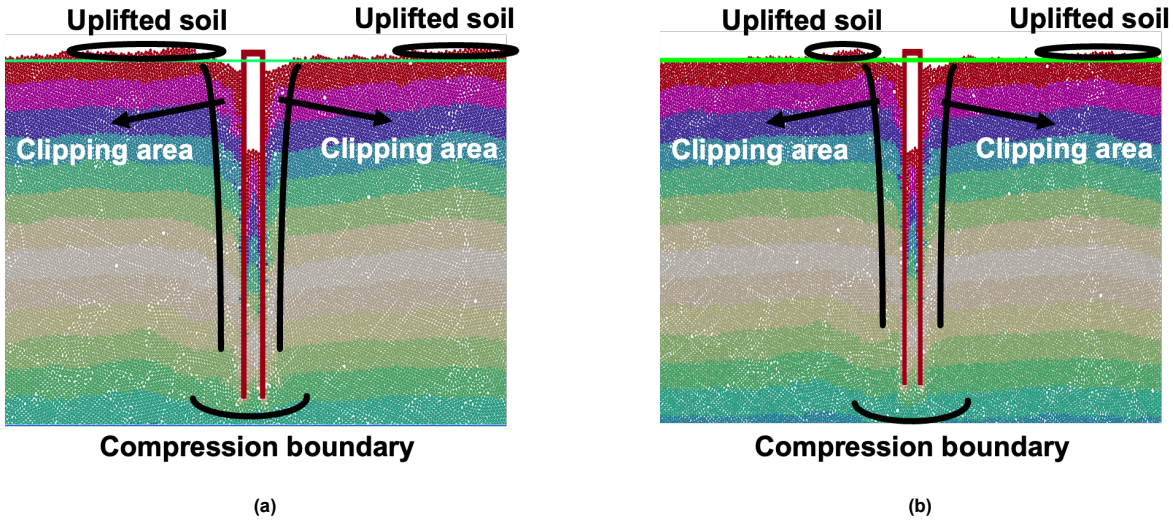

Figure 4.2: Final state after pile installation (green line represents soil surface level before self-weight penetration): (a) Jacking; (b) Impact driving

One of the most important results from pile installation simulation is penetration resistance evolution over depth. In order to visualize the force evolution trend more clearly, we also apply the moving average method to smooth the result. The result after post-processing is shown in Figure 4.3.

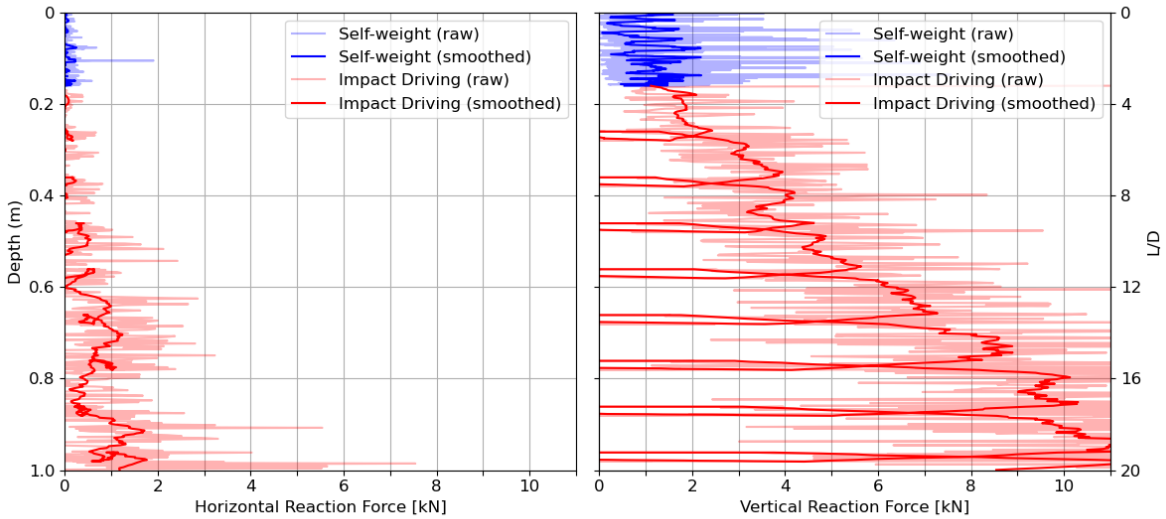

Figure 4.3: Penetration resistance evolution over time of impact driving

Comparing Figure 4.3 and Figure 3.10(a), it can be seen that both installation methods ultimately reach a similar magnitude of penetration resistance (approximately $10kN$ to $11kN$). However, their vertical force–depth profiles show notable differences due to the fundamentally distinct loading mechanisms involved.

In the case of impact driving, both horizontal and vertical reaction force curves exhibit strong oscillations and multiple local peaks. This matches with the impact driving velocity function we made to represent the hammering process, which contains 8 blows until the pile is fully installed. During the hammering phase, the sudden movement of the pile (hammering) will cause a rapid jump of the vertical reaction force, and at the rebounding phase, in which the pile moves upward for a small amount of distance, the pile will experience an inverse shaft friction, and the tip resistance will become zero after an instant of time, leading to the rapid drop of the vertical reaction force in the plot. Moreover, the accumulated vertical reaction force is a result of the densification of soil underneath the pile tip; with the pile penetrating deeper into the soil, the soil tends to become denser under the influence of the pile tip, leading to higher penetration resistance.

Comparing with the jacking plot, the difference is easy to observe; the jacking vertical reaction force keeps accumulating during pile installation. This reflects the quasi-static loading condition, where side friction and base resistance develop progressively as the pile penetrates the soil.

4.2. Vibratory Driving Simulation

Comparing with other installation methods, vibratory driving is a more flexible and environmentally friendly pile installation method. The nature of the vibratory driving method allows piles to be installed in hard soil layers and near highly sensitive structures. Moreover, the biggest advantage of vibratory driving is its low noise production [51]. For example, during impact piling, a hammer strikes the top of a steel pile and this impact transmits sound into the air, water, and sediment. This creates very high impulse noise that can be heard even several kilometers away from the construction site. But for vibratory driving, even though it also produces noise to some extent, the sound generated from vibratory pile driving is classified as more non-impulsive, continuous sound, which causes less influence on the environment and local animals or plants.

4.2.1. Simulation campaign

Firstly, the vibratory driving method is used to investigate the influence of installation methods. The initial state before installing the pile is used as after self-weight penetration in chapter 4.

When it comes to boundary conditions, the left, right, and bottom walls are still fixed. The gravity field is kept activated, while the pile is driven by controlling the vertical velocity, and the horizontal and rotating movements are restricted. In this simulation, the pile is also installed into the soil by 1 meter (pile length), which is the same as the penetration depth in the jacking simulation. For numerical stability and efficiency, two frequency values of vibratory driving are picked as $4Hz$ and $10Hz$ respectively in this case, which are considered to be enough for representing the vibratory driving method.

The working principle of vibratory pile driving is to reduce the ground resistance by vibrating the pile and then driving the pile into the soil. In this simulation, the vertical velocity of the pile is prescribed as a combination of a constant downward component and a harmonic oscillation. Specifically, the velocity is defined as:

$$v(t) = -\left(v_0 + A \cdot \omega \cdot \cos(\omega t)\right) \tag{4.1}$$

where $v_0 = 0.02\,\text{m/s}$ is the offset velocity ensuring continuous penetration, $A = 0.006\,\text{m}$ is the vibration amplitude, and $\omega = 2\pi f$ is the angular frequency corresponding to the vibration frequency. The negative sign ensures the motion is directed downward in the global coordinate system.

Table 4.2: Parameters used in the vibratory driving simulations at 4 Hz and 10 Hz

Property	Value (4 Hz)	Value (10 Hz)	Unit
Frequency	4	10	Hz
Amplitude	0.006	0.006	m
Offset velocity	0.02	0.02	m/s

4.2.2. Simulation results

For pile installation methods simulation, one of the most important things is penetration resistance, which is the vertical reaction force in this case. Considering the high-frequency change in velocity as

well as the number of records, the moving average method is applied to smooth the result for better visualization. The results for $4Hz$ and $10Hz$ after smoothing are shown in Figure 4.4 and Figure 4.5.

Comparing those two figures above and Figure 3.10(a), it is clear that after pile installation, the jacking method can reach approximately $10kN$ to $11kN$ penetration resistance, while vibratory driving has only around $5kN$ to $6kN$ penetration resistance. Moreover, compared with jacking, the vertical reaction force shows more obvious fluctuations, which are consistent with the characteristics of this installation method because the movement speed of the pile is defined by a simple harmonic function.

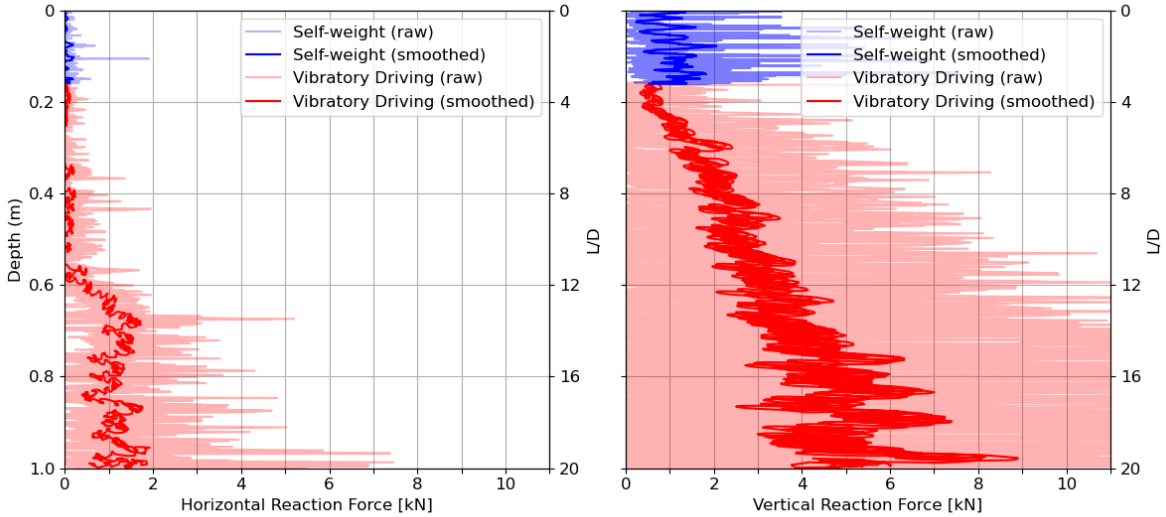

Figure 4.4: Penetration resistance evolution over time of $4Hz$ vibratory driving

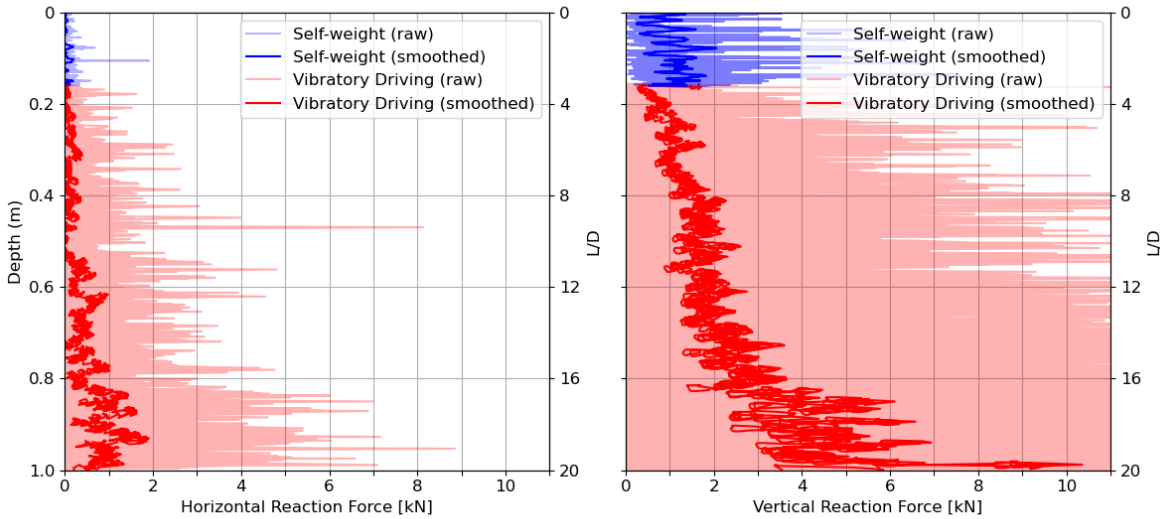

Figure 4.5: Penetration resistance evolution over time of $10Hz$ vibratory driving

The soil behavior during pile installation should be observed and compared with the other two methods. In order to compare the difference between these four installation methods, the soil final states after installation for jacking, impact driving, vibratory driving with $4Hz$ frequency, and $10Hz$ frequency are shown respectively in Figure 4.6. In this comparison, the soil behavior during different installation methods will be investigated roughly by viewing the final states; in the later parts of this chapter, they

will also be compared quantitatively in order to have a more direct concept of the difference between each installation method.

From Figure 4.6, it is clear that the clipping area, uplifted soil, and compression boundary which can be observed in both jacking and impact driving can also be observed in vibratory driving. When looking into detail, it can be observed that the soil uplifting for vibratory driving, especially for $10Hz$ frequency, is much smaller than jacking and impact driving. This may be caused by the soil densification effect of vibration. During the vibratory driving process, the oscillatory motion of the pile reduces inter-particle friction and allows soil grains to rearrange into a denser configuration, which means that fewer soil particles will be uplifted. When comparing with the green line, on the right side close to the pile, it can be seen that the soil settles down after pile installation; the only uplifted soil appears far away from the pile. This asymmetric behavior is probably caused by the radius of particle we used in this model. Moreover, the compression boundary for the vibratory driving pile is slightly deeper than the other two methods, especially comparing to jacking method. This is also caused by the denser configuration in the vibratory model, which further explains the more serious densification effect of vibratory driving. All behaviors reflect that vibratory driving has less soil uplifting, and denser particle layout, and this effect tends to increase with higher frequency.

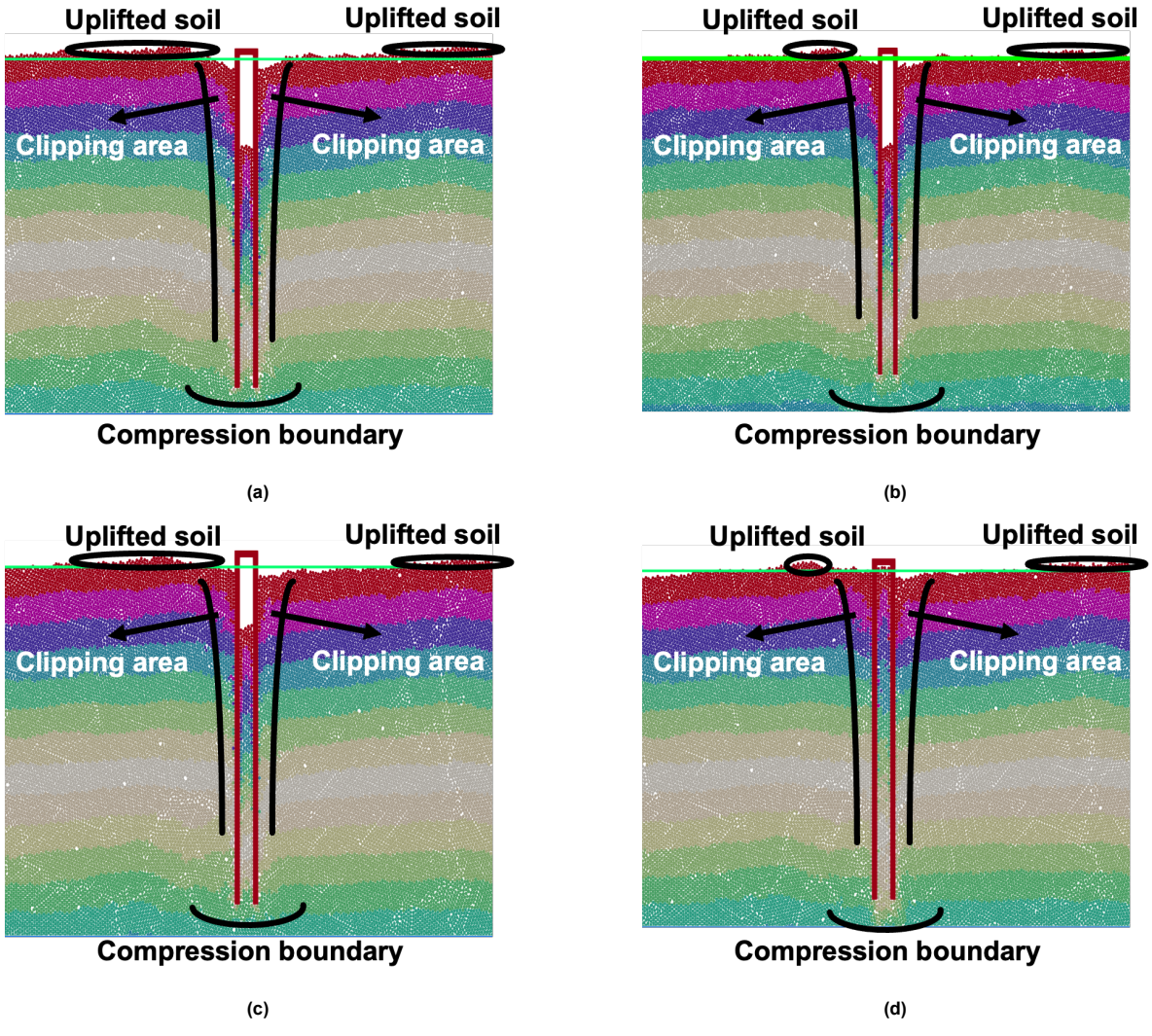

Figure 4.6: Final states during pile installation (green line represents soil surface level before self-weight penetration): (a) Jacking; (b) Impact driving; (c) Vibratory driving with 4Hz frequency; (d) Vibratory driving with 10Hz frequency

4.3. Comparison Among Different Methods

In order to find the influence of different installation methods, as well as finding an optimal way for pile installation, it is necessary to compare various results among these installation methods.

4.3.1. Penetration resistance

One of the most important results for pile installation is penetration resistance. The reaction force evolution with pile penetration depth as well as the dimensionless parameter L/D is shown in Figure 4.7. In order to more intuitively compare the penetration resistance of different installation methods at different penetration depths, we draw four curves in Figure 4.8 to show the penetration resistance of different installation methods at the time when L/D equals 4, 8, 12, 16, and 20, respectively.

From the two plots, it is clear that vibratory driving with a frequency of $10Hz$ has the lowest penetration resistance during the pile installation process, while impact driving leads to the highest value. When looking into detail, for jacking and vibratory driving, the overall evolution trend is increasing, with a small decrease at $L/D = 16$ for jacking. This may be because of the fluctuation behavior of the penetration resistance, which causes a sudden decrease at this time point.

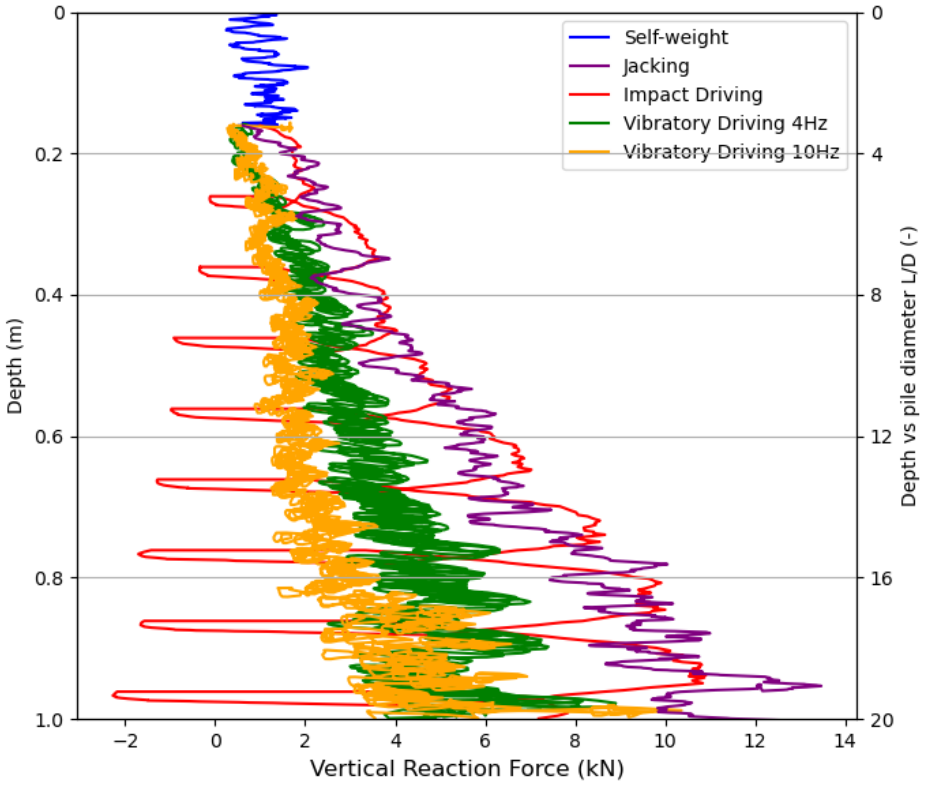

Figure 4.7: Comparison of penetration resistance among three installation methods

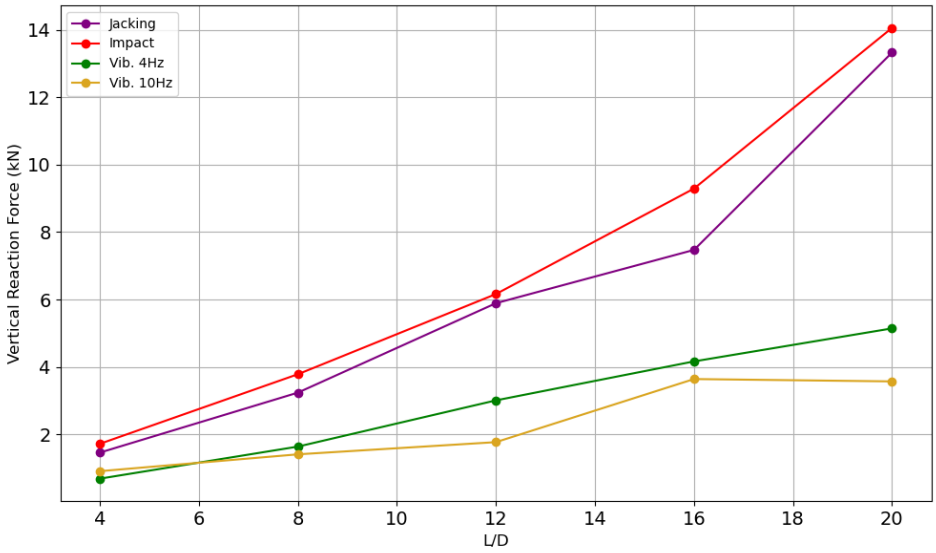

Figure 4.8: Normalized reaction forces for different installation methods at different L/D

4.3.2. Soil densification after pile installation

During the pile driving process, the soil around and inside the pile will be densified, which has an influence on the shaft friction and tip resistance of the pile. In order to evaluate the soil densification, soil displacement distribution for each method can be used to compare the soil densification effect of pile driving methods. As a standard situation, the soil displacement distribution before pile self-weight penetration is used as an initial state.

In order to compare the change in soil displacement distribution within the model, the positions of every single soil particle are determined after each stage, including self-weight penetration, jacking, impact driving, vibratory driving with $4Hz$ frequency and vibratory driving with $10Hz$. After that, each state is used to compare with the reference state, which is before self-weight penetration. The absolute displacement of soil particles is calculated from the change in particle positions and it is normalized by dividing it by the pile inner diameter. Because in this study, we are mostly interested in the soil densification effect around the pile shaft, only $1.2m$ in width area is plotted in this part. The contour maps of displacement are shown in Figure 4.9. In the contour map, larger displacement represents more serious soil densification, and smaller value stands for less serious densification effect. In Figure 4.9(b), the jacking method induces minimal disturbance, with moderate densification around the pile due to localized shearing and compaction. In contrast, impact driving causes more pronounced rearrangement of the soil structure, resulting in observable densification along the pile and mild loosening inside the pile due to soil displacement. Vibratory driving exhibits a broader zone of densification around the pile, suggesting effective particle rearrangement and compaction induced by vibratory driving. These results indicate that vibratory driving enhances soil densification more significantly than jacking or impact methods.

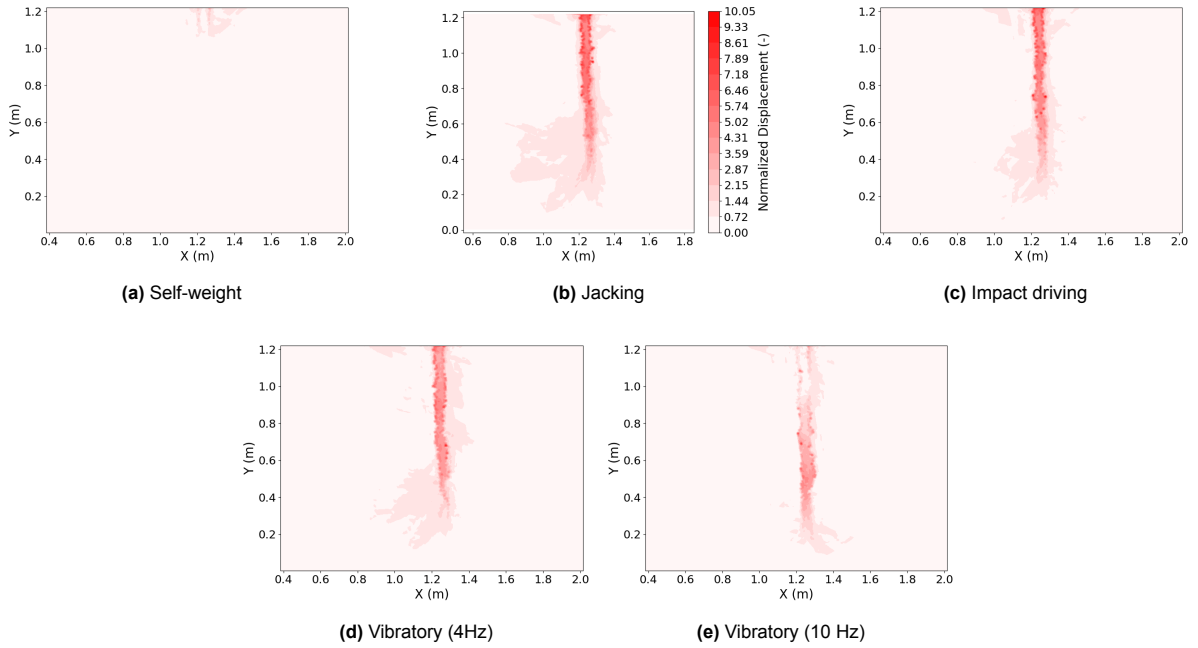

(a) Self-weight **(b)** Jacking **(c)** Impact driving

(d) Vibratory (4Hz) **(e)** Vibratory (10 Hz)

Figure 4.9: Comparison of results for five different installation methods with density changes after the sample stabilization stage: (a) self-weight, (b) jacking, (c) impact driving, (d) vibratory driving with 4Hz frequency, and (e) vibratory driving with 10Hz frequency.

4.3.3. Soil plug and uplifting

For hollow pile installation, due to the soil squeezing effect and the frictional resistance of the inner wall of the pile, soil uplifting on both sides of the pile and a soil plug inside the pile will occur during the installation process. These are important manifestations of pile installation.

The *Incremental Filling Ratio* (IFR) and *Plug Length Ratio* (PLR) are two important dimensionless parameters commonly used to characterize the development of soil plugging in open-ended piles during installation. These indices provide complementary perspectives on the extent and evolution of the soil plug formation.

The IFR quantifies the proportion of incremental pile penetration that is occupied by soil, effectively reflecting the dynamic response of soil infill relative to the pile movement. It is defined as:

$$\mathrm{IFR} = \frac{\Delta h}{\Delta L}$$

where Δh is the incremental increase in the height of soil inside the pile, and ΔL is the incremental penetration depth of the pile. A higher IFR value indicates a more dominant plugging behavior during that penetration increment.

In contrast, the PLR measures the relative length of the accumulated soil plug inside the pile with respect to the total embedded length of the pile. It provides a cumulative view of the plugging state throughout the installation process. PLR is defined as:

$$\mathrm{PLR} = \frac{h}{L}$$

where h is the total height of soil inside the pile, and L is the total penetration depth of the pile at a given moment. A PLR approaching unity suggests a fully plugged condition, whereas a lower PLR indicates a more coring or unplugged behavior.

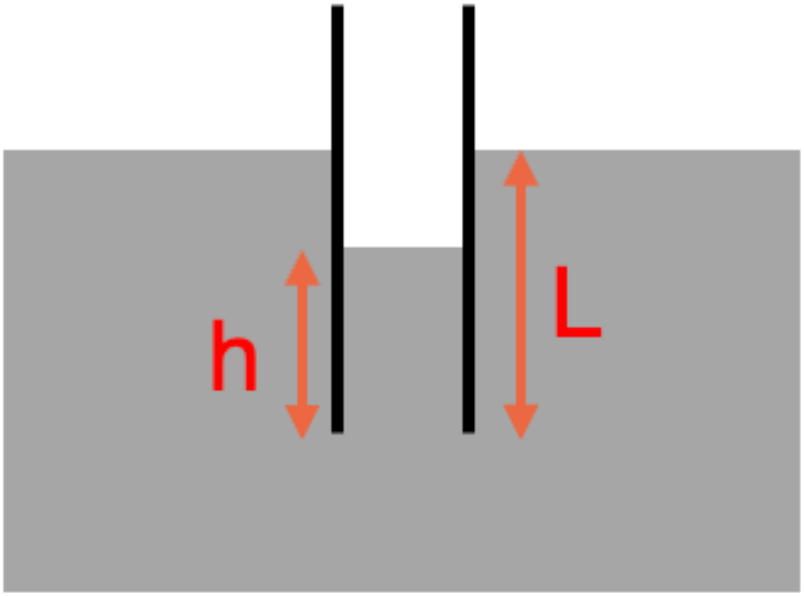

Figure 4.10: Soil plug length h and pile penetration depth L

The evolutions of PLR and IFR during pile installation are illustrated in Figure 4.11 and Figure 4.12, offering insights into the temporal and spatial variations of the soil plug formation mechanisms.

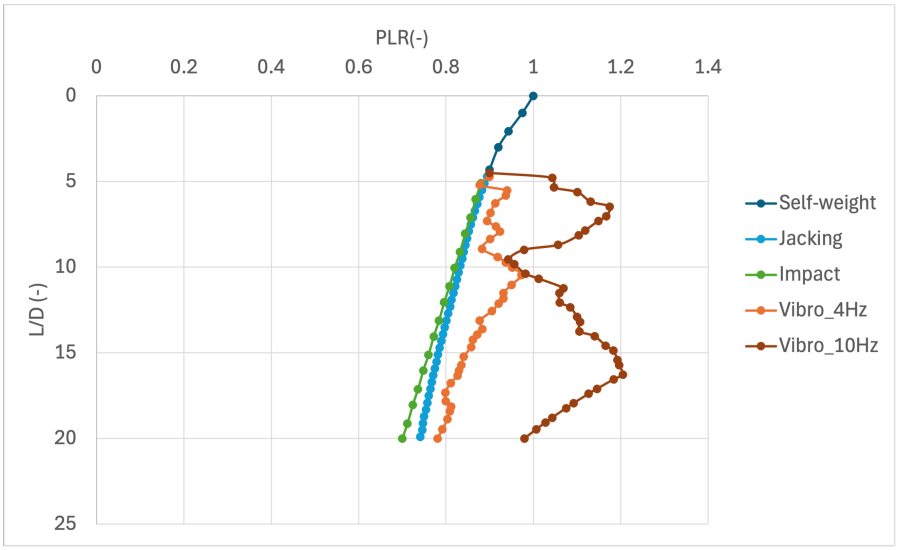

Figure 4.11: PLR evolution during pile penetration

From Figure 4.11, it can be seen that vibratory driving will lead to the highest PLR value, which means that the longest soil plug will form during this pile installation method; meanwhile, the impact-driven pile has the lowest PLR, meaning that the shortest soil plugs appear in this method. Moreover, comparing vibratory driving with 2 different frequencies, it is clear that $10Hz$ vibratory driving pile has a much more significant soil plug effect, which can be attributed to the higher vibration frequency inducing more continuous and rapid cyclic loading, thereby enhancing the rearrangement and movement of soil particles, resulting in a longer soil plug inside the pile.

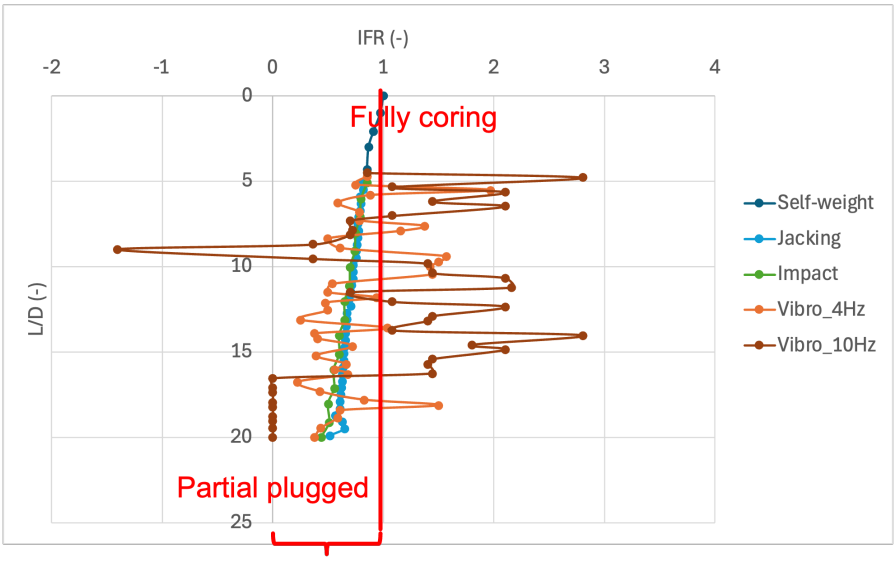

Figure 4.12: IFR evolution during pile penetration

When comparing the IFR evolution during different pile installation methods, it can be seen in Figure 4.12 that, except for the jacking method, the other three installation methods all show significant oscillation during pile driving. The final 0 IFR values for $10Hz$ vibratory driving are because the pile is not long enough to contain all the soil plug, so it stops increasing when the pile is fully filled with soil inside.

It is worth noting that in vibratory with $10Hz$ frequency simulation, most of the time the PLR value is larger than 1, which is physically unrealistic. This phenomenon is likely attributed to the relatively low inter-particle friction coefficient adopted in the DEM model ($\mu = 0.1$). A low friction coefficient reduces the shear resistance between particles, facilitating excessive relative movement and rearrangement of soil particles. As a result, the soil can enter and accumulate within the pile faster than in real conditions, leading to an overestimation of the plug height and thus artificially inflated PLR values. Also, the small inner diameter of the pile and the big soil particle radius may also influence the soil plug formation. Inside the model pile, each row of soil particles can only contain a maximum of 5 soil particles, which means that the length of the soil plug will grow rapidly due to the insufficient capacity of the pile. To mitigate this artifact, future studies should consider employing a higher particle friction coefficient, a larger pile diameter as well as a smaller particle radius that better reflects the real pile installation process.

In order to know the influence of the friction coefficient (μ), simulations of jacking, impact driving, and vibratory driving with 4 Hz frequency were performed again to investigate the change in PLR and IFR. The comparison of these parameters is shown in Figure 4.13, Figure 4.14 and Figure 4.15.

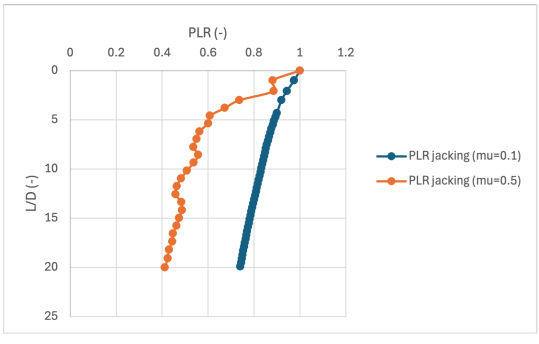

(a) PLR comparison

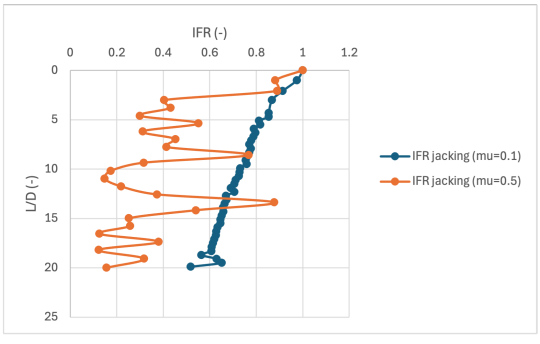

(b) IFR comparison

Figure 4.13: PLR and IFR comparison for different μ (jacking)

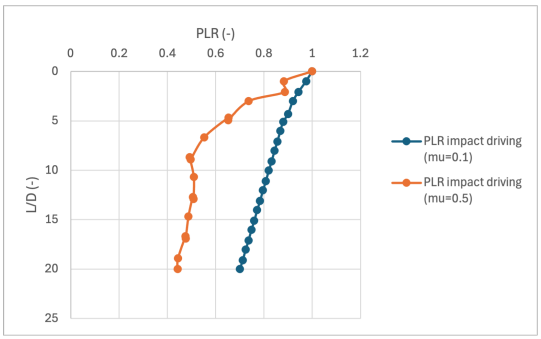

(a) PLR comparison

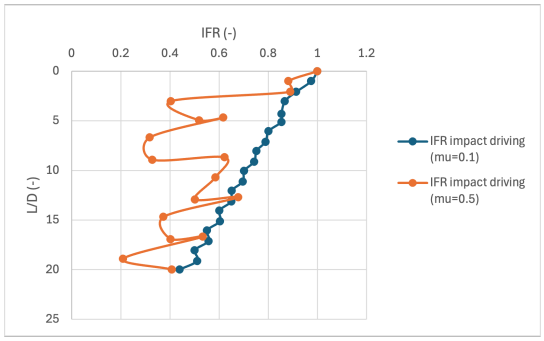

(b) IFR comparison

Figure 4.14: PLR and IFR comparison for different μ (impact driving)

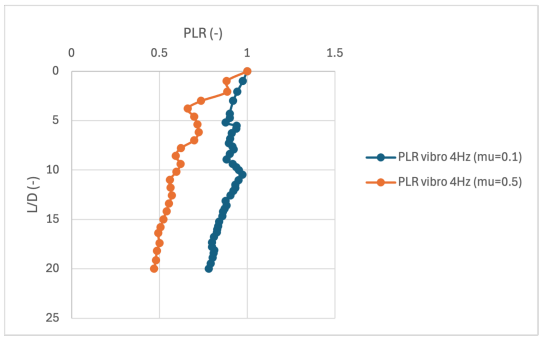

(a) PLR comparison

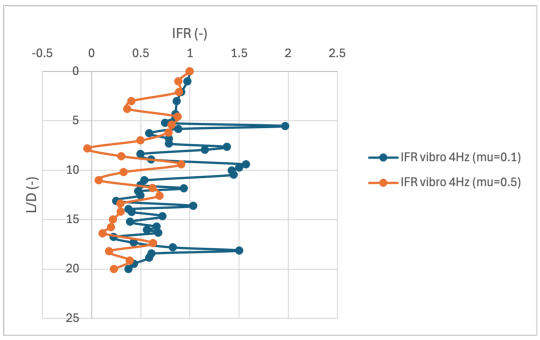

(b) IFR comparison

Figure 4.15: PLR and IFR comparison for different μ (vibratory driving with 4 Hz)

From these plots, it is clear that when using a higher μ, both PLR and IFR are lower than using smaller μ, which means that by changing the coefficient of friction to a more realistic value, the problem of unrealistic soil plug length can be mitigated.

Furthermore, the uplifting of soil during penetration is measured by searching for the highest y-coordinate of soil particles during penetration. The soil uplifting on the left and right sides of the pile is investigated separately in this study. First, the highest y-coordinate of soil particles is recorded, and then the difference between this value and the soil level after the self-weight penetration process is calculated, which is called Δh. This value is then normalized by dividing it by the penetration depth L and smoothed by using a moving average method with a window size of 5. The results for different installation methods are shown in Figure 4.17, in which the solid line represents the left-hand side of the pile, while the dashed line stands for the right-hand side of the pile.

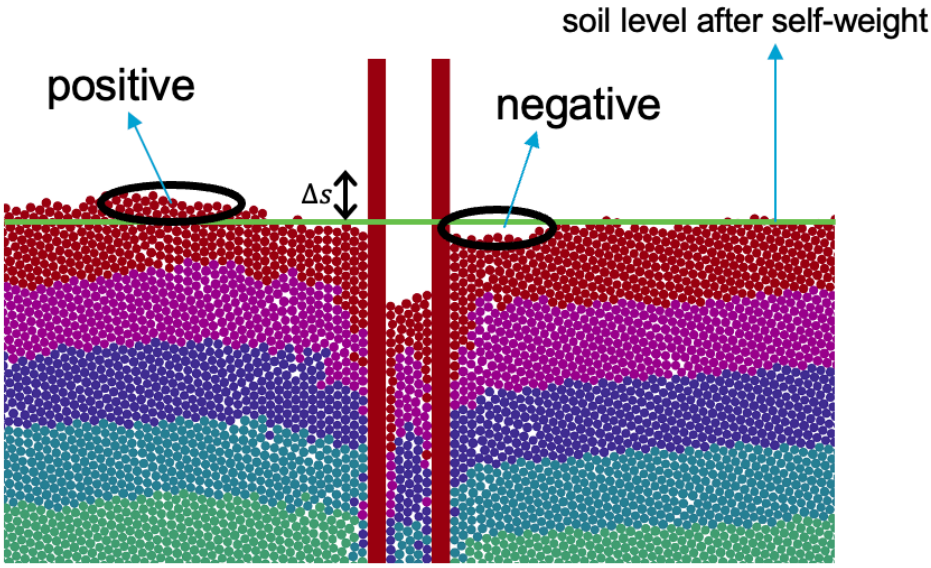

Figure 4.16: Schematic representation of soil uplifting

The simulation results reveal notable differences in soil uplift behavior induced by different pile installation methods. Among all methods, impact driving produces the most significant uplift of surrounding soil, followed by jacking, while vibratory driving induces the least amount of uplift. Furthermore, vibratory driving at 10 Hz results in even lower uplift compared to the 4 Hz case. These observations can be attributed to the mechanism and energy transfer associated with each method: impact driving transmits impulsive and concentrated energy, causing considerable upward displacement of nearby soil; jacking applies relatively steady pressure, leading to moderate uplift; vibratory driving, especially at higher frequencies, facilitates soil rearrangement and compaction, thereby suppressing upward movement. This soil uplifting behavior can also be explained by the soil plug formation. Impact driving has the smallest amount of soil plug, while vibratory driving has the largest, because more soil particles move into the pile instead of being uplifted.

Additionally, lateral asymmetry in the uplift distribution is observed. For impact driving and vibratory driving at 4 Hz, the left side of the pile exhibits greater uplift than the right, whereas for jacking and vibratory driving at 10 Hz, the right side shows more pronounced uplift. These asymmetries may stem from the large particle radius used in this study, which is also observed and discussed in the previous comparison of four installation methods. Most notably, for the 4 Hz and 10 Hz vibratory driving cases, the uplift values remain negative throughout much of the installation process, indicating settlement rather than uplift. This significant settlement behavior not only comes from the soil densification and particle rearrangement under vibratory driving, but also due to the large amount of soil plug inside the pile.

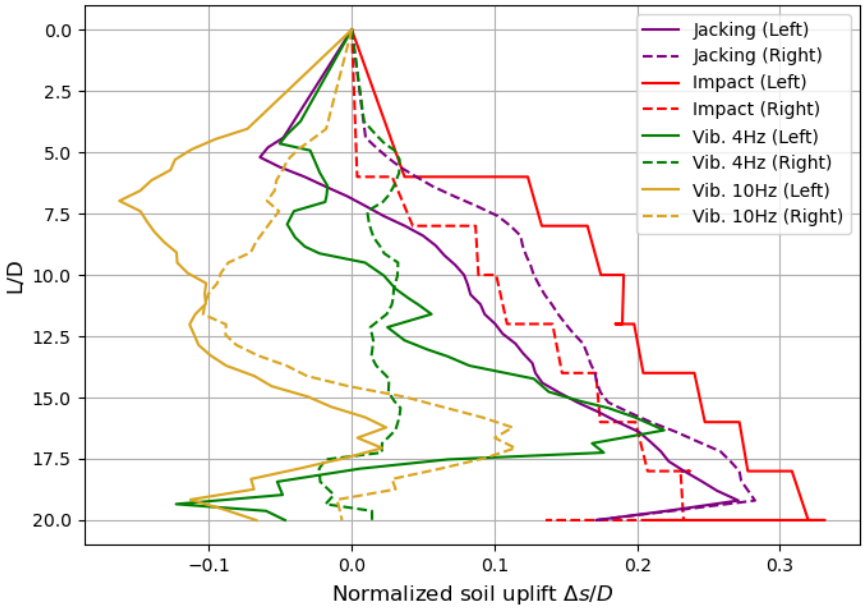

Figure 4.17: Soil uplifting during different pile installation methods

4.4. Conclusion

This chapter presented a comprehensive numerical investigation of three pile installation methods: impact driving and vibratory driving at 4Hz and 10Hz, based on the validated model introduced in Chapter 4. These methods were systematically compared against the jacking method to evaluate their influence on penetration resistance, soil densification, soil plug formation, and soil uplifting.

The simulation results demonstrate that each installation method induces distinct soil-structure interaction behaviors. Impact driving generates the highest penetration resistance, owing to its concentrated impulsive energy, and leads to the most significant soil uplifting, as the vertical stress waves promote upward displacement of soil particles. Jacking, characterized by a quasi-static loading scheme, yields moderate resistance and uplift. In contrast, vibratory driving, particularly at 10 Hz frequency, significantly reduces penetration resistance and results in the lowest level of soil uplift, sometimes even causing settlement due to soil densification.

Vibratory driving is also the most effective in promoting soil plug formation, with the highest observed values of Plug Length Ratio (PLR) and Incremental Filling Ratio (IFR), especially at 10 Hz. The high-frequency cyclic loading enhances particle rearrangement and confinement within the pile, contributing to a longer soil plug. This contrasts with impact driving, where the impulsive nature of the load results in limited soil plug development and shorter plug lengths. The extent of soil uplifting is also closely linked to the degree of soil plug formation. Methods that form longer plugs tend to reduce soil uplift, as more soil enters the pile instead of being displaced upward.

Furthermore, vibratory driving induces more densification of the surrounding soil compared to the other methods, which is beneficial for improving shaft resistance and long-term performance.

In addition to its mechanical advantages, vibratory driving offers environmental benefits. It generates less noise pollution compared to impact driving, which is critical for offshore and environmentally sensitive applications. Considering all aspects, including penetration efficiency, soil response, plug development, and environmental effect, vibratory driving emerges as the most advantageous method for offshore pile installation.

5

Pull-out Resistance for Different Methods

While floating offshore wind turbines are increasingly deployed in deep-sea environments, the geotechnical performance of their anchoring systems remains insufficiently explored, especially in the area of numerical simulation. In particular, the piles used to anchor mooring lines are typically subjected to inclined tensile loading, which deviates significantly from the vertical or compressive loading scenarios considered in conventional pile design. Although various anchoring techniques—such as suction piles, drag anchors, and driven open-ended piles—have been adopted in practice, the understanding of their pull-out behavior under inclined loads remains limited. Most existing studies only focus on pull-out methods, and the influence of different pile installation methods on pull-out resistance is rarely addressed. Therefore, this chapter investigates the pull-out capacity of piles installed using different techniques and subjected to various loading angles, in order to provide insight into the design of efficient anchoring systems for floating offshore wind applications.

5.1. Simulation campaign

In order to represent the pile pull-out process, a small disk (we call it ‘connector‘ in this study) with a radius only one-tenth the radius of the smallest soil particle is added on the top of the pile, while the x-coordinate is exactly at the center of the pile. There is also a small distance ($0.0165m$, 3 times the largest particle radius) in the y-direction between the pile top wall and the connector, which is used to represent an elastic connection (usually a mooring line in practical operation) between the connector and the pile. The reason why we did not apply the velocity directly to the pile is that the pile is modeled as a rigid body, so that the velocity can only be applied to the center of mass of the pile, which makes the extraction behavior unrealistic compared to the real construction. In order to make sure that the pile movement can be fully controlled by the connector, we apply unrealistically high stiffness to the elastic connection. In this stage, the pile is free in horizontal, vertical, and rotational directions, in order to make the pile move freely in the area, thus investigating more into the pulling capacity of the pile.

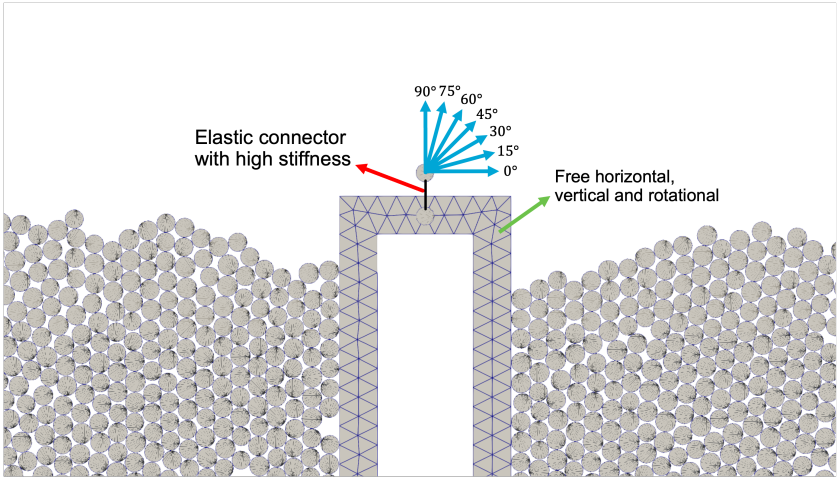

Figure 5.1: Boundary conditions for pile pull-out simulation

Considering the simulation efficiency, only jacking, impact driving, and vibratory driving with $4Hz$ frequency models are used to perform the pull-out simulation. In the previous research, only a small number of researchers investigated the influence of the velocity angle of pile pull-out, so that in this study we apply five different angles of velocity to investigate the difference in pull-out capacity, $0°$, $15°$, $30°$, $45°$, $60°$, $75°$, and $90°$, respectively. For each velocity angle, the total amount of velocity values is always kept $0.01m/s$, which was used by Huang et al. in 2020 [52]. In the research of Huang et al., they used velocity as $0.1mm/s$, but in the gravity field of 100 g, which means that in this study, according to the dimensional analysis, the velocity can be 100 times larger, which is $0.01m/s$.

It is also important to note that the connector is positioned above the pile top and connected through an elastic line, which introduces a vertical offset in the application point of the pulling force. As a result, during inclined pull-out scenarios, the loading is applied with a lever relative to the center of mass of the pile, inevitably inducing a moment on the pile. This induced moment may cause additional rotation or lateral displacement of the pile, especially under large inclination angles. In future refinements, alternative loading strategies—such as applying force directly at the pile head through distributed contact points—could be explored to reduce the influence of the induced moment and isolate axial resistance more clearly.

5.2. Dimensional Analysis

Dimensional analysis is a fundamental technique used to reduce the number of governing variables in a physical system and to identify the dimensionless groups that control its behavior. By applying the Buckingham π theorem, the original variables can be transformed into a smaller set of dimensionless quantities that preserve the system's fundamental physics [53].

In the context of pile pull-out simulation, because the objective is to further validate the numerical results against existing centrifuge tests, dimensional analysis is useful for canceling out the effects of different material properties such as pile diameter, soil density, and pile penetration depth. In this study, the pull-out force P_u is selected as the sole dependent variable, and it is assumed to depend on six independent variables: pile length L, diameter D, installation velocity v, gravitational acceleration g, bulk density of soil ρ_{bulk}, and the pull-out angle β.

The dimensional properties of these variables are summarized in Table 5.1. By selecting ρ_{bulk}, D, and v as the repeating variables and applying the Buckingham π theorem, four independent dimensionless groups that fully describe the system can be obtained.

Table 5.1: List of variables and their physical dimensions

Variable	Meaning	Dimension
P_u	Pull-out force	MLT^{-2}
L, D	Pile length and diameter	L
g	Gravitational acceleration	LT^{-2}
ρ_{bulk}	Bulk density of soil	ML^{-3}
v	Installation velocity	LT^{-1}
β	Pull-out angle	Dimensionless

The resulting dimensionless groups are listed in Table 5.2.

Table 5.2: Dimensionless groups derived from the Buckingham π theorem

Dimensionless Group	Expression
π_1	$P_u/(\rho_{\text{bulk}} D^2 v^2)$
π_2	L/D
π_3	gD/v^2
π_4	β

Here, π_1 represents the normalized pull-out force, which is analogous to a dynamic force coefficient. π_2 is the slenderness ratio of the pile, which influences the development of shaft friction and end bearing. π_3 compares gravitational effects to inertial effects and can be interpreted as a Froude-type number. Finally, π_4 characterizes the interface friction between the pile and surrounding soil.

Accordingly, the normalized pull-out force can be expressed as a function of the remaining dimensionless groups:

$$\frac{P_u}{\rho_{\text{bulk}} D^2 v^2} = f\left(\beta, \frac{gD}{v^2}, \frac{L}{D}\right)$$

It is worth noting that, for simplicity, this thesis considers only one dependent variable and six independent variables. However, in practical research problems, additional variables such as the friction coefficient, pile thickness, and pile stiffness may also influence the dependent variable, and these will be the focus of future studies.

5.3. Results

First of all, the pull-out capacity values of each method with different pulling angles should be determined. The vertical and horizontal reaction forces on the connector are detected during the pull-out process. The results are shown below. In the plots, the pile vertical displacement is represented by the dimensionless parameter L/D, which is helpful for removing the influence of the scale effect. The resultant pull-out force F was calculated as the vector magnitude of its orthogonal components, i.e., $F = \sqrt{F_x^2 + F_y^2}$, where F_x and F_y are the horizontal and vertical components that are recorded on the connector.

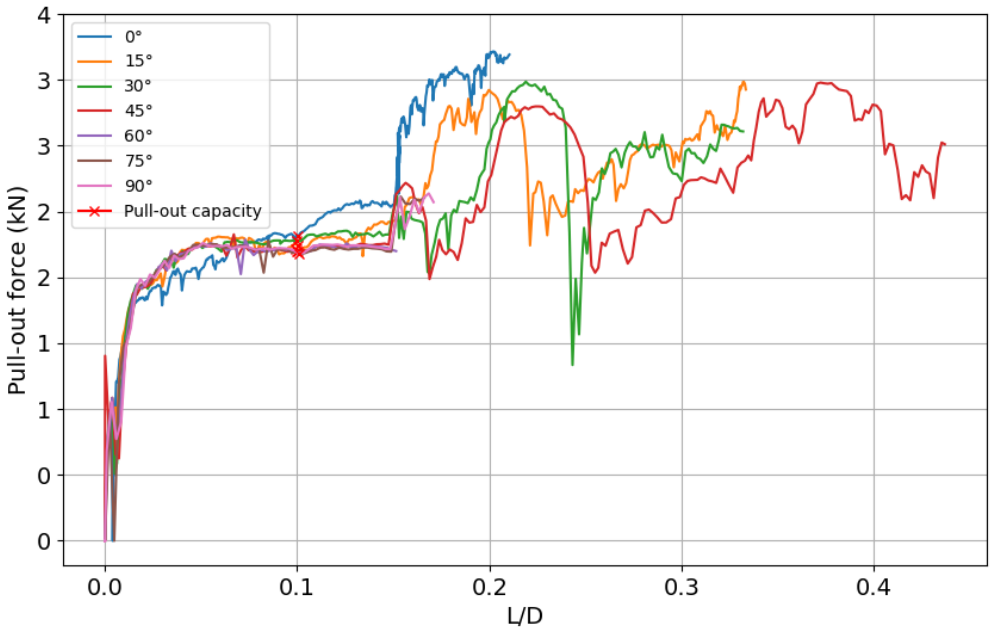

Figure 5.2: Pull-out forces after jacking

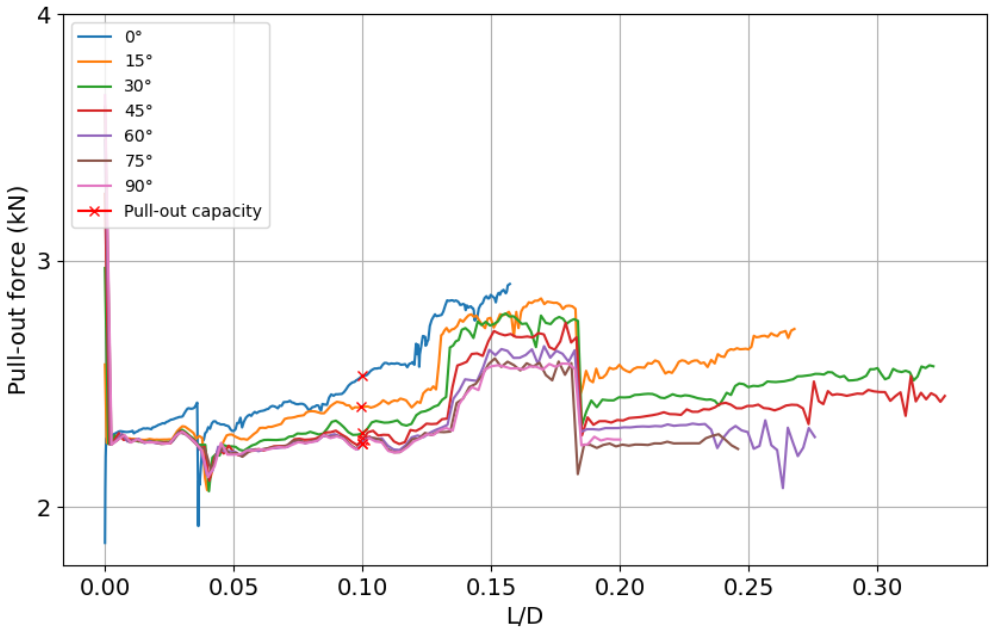

Figure 5.3: Impact driving pull-out forces

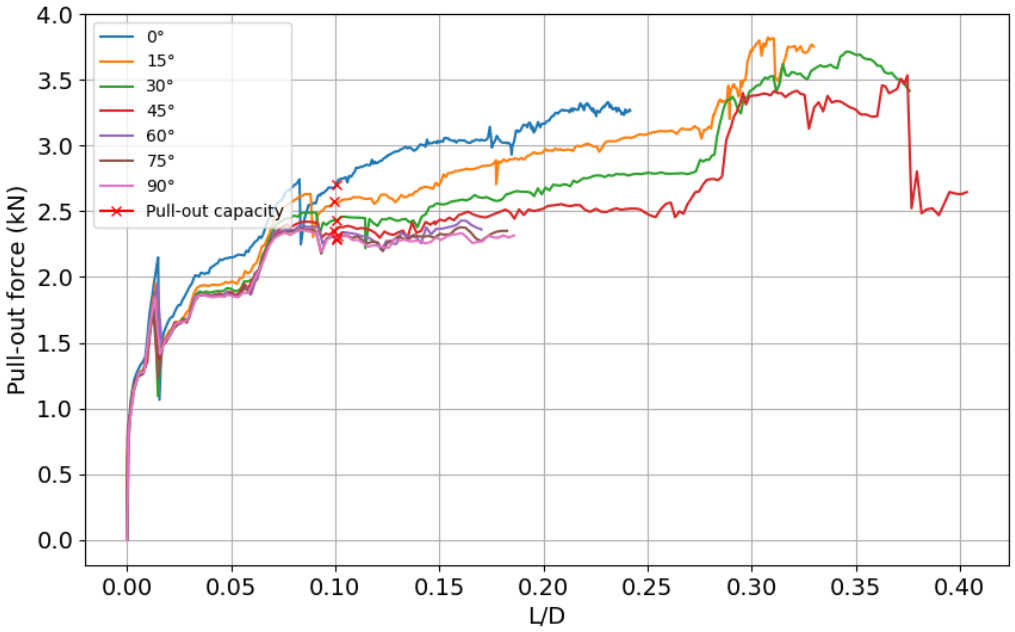

Figure 5.4: Vibratory driving pull-out forces

According to Burd et al. (2020), the ultimate response of a pile is determined at 0.1 L/D, differentiating between the small and large displacements between the soil and pile [54]. For this reason, the simulation results of the three installation methods, we use the F value corresponding to $L/D = 0.1$ as the pull-out capacity and mark it in the plots using the red cross. At $L/D = 0.1$, it can be seen that the curves reach a flat part, which means that the displacement of the pile increases much faster than the pull-out force increases. During the pile pull-out process, a second or even third loading increase will happen to the pile load, but this is because during pile inclined loading, the soil in the horizontal direction will be densified due to the horizontal component of the pull-out force, thus providing extra resistance to pile extraction, so that picking the time when $L/D = 0.1$ as the pull-out capacity is reasonable and comparable among installation methods.

Figure 5.2 illustrates the variation of pile load F with normalized displacement L/D under different inclination angles during the pull-out process of a jacked pile. Initially, a sharp increase in pile load is observed across all angles, which is considered to be caused by the mobilization of skin friction at the initial stage of pile pull-out. This increase is followed by a transient drop in pile load, which may be attributed to local failure of soil structure near the pile due to shaft friction, or sudden loss of tip resistance as the pile begins to move. Following this, the pile load exhibits a gradual increase, and then starts stabilizing as the normalized displacement progresses. This quasi-steady stage reflects a balance between continuous soil yielding and interface shearing between pile and soil body. Notably, the peak pull-out resistance varies with inclination angle: lower angles (e.g., $0°$–$30°$) tend to exhibit slightly higher ultimate capacities, whereas steeper angles demonstrate reduced capacity; this is also reasonable due to the increase in horizontal movement, which means that the soil body at the right side of the pile will provide additional support to the pile, causing more force to move the pile out of the soil body. The consistent progression and stabilization of force after the initial change imply a resilient load-transfer mechanism governed by progressive mobilization rather than brittle failure.

Figure 5.3 shows the pull-out simulation results for piles installed by the impact driving method. Except for $0°$ angle simulation, a consistent pattern is observed across all other angles: the pile load starts from a rather high value, followed by a rapid drop, and then experiences a long-time constant stage, followed by a gradual rise toward a steady-state capacity; after the short-time stable progression, the pile load shows a trend of decrease. This behavior reflects the transient dynamic response at the beginning of loading, likely due to rapid mobilization and local structural effects. As the inclination angle increases, the peak pull-out capacity tends to decrease, indicating that higher angles will lead to more

soil on the right side of the pile contributing to resistance. What is worth noticing is that, for 0° pull-out angle, the pile load shows different behavior. Initially, the load starts from a small value, then increases rapidly until the end of decrease in other models; after that, rather than staying constant for a long period of time, the load value continues to increase at a much lower speed. When the pile load for other models starts increasing rapidly, the 0° model behaves the same as others until the end of the pull-out simulation. This behavior may be caused by the nature of horizontal load; the external load not only needs to encounter the self-weight of the pile, shaft friction, and base resistance, but also the weight of side soil will provide a large amount of counter force in this case, which leads to the increase mode of progress.

The pull-out responses for piles installed using vibratory driving under various inclination angles are presented in Figure 5.4. As in jacked pile pull-out simulation, all curves start from 0 pile load, then exhibit a rapid initial rise, followed by a sharp peak and then drop rapidly to around half of the peak value. After that, the pile load starts increasing continuously until another peak value, then another drop-rise process happens again. These oscillations probably reflect the breakage of soil nearby, as vibratory driving tends to disturb the surrounding soil more significantly. During pile pull-out, the movement of the pile may influence the surrounding soil further, leading to damage of soil structure, thus causing a rapid drop in shaft friction. As is shown in the previous two series of simulations, the pull-out capacity decreases with increasing inclination angle, suggesting that a smaller loading angle will lead to higher pull-out capacity due to the additional support provided by the surrounding soil.

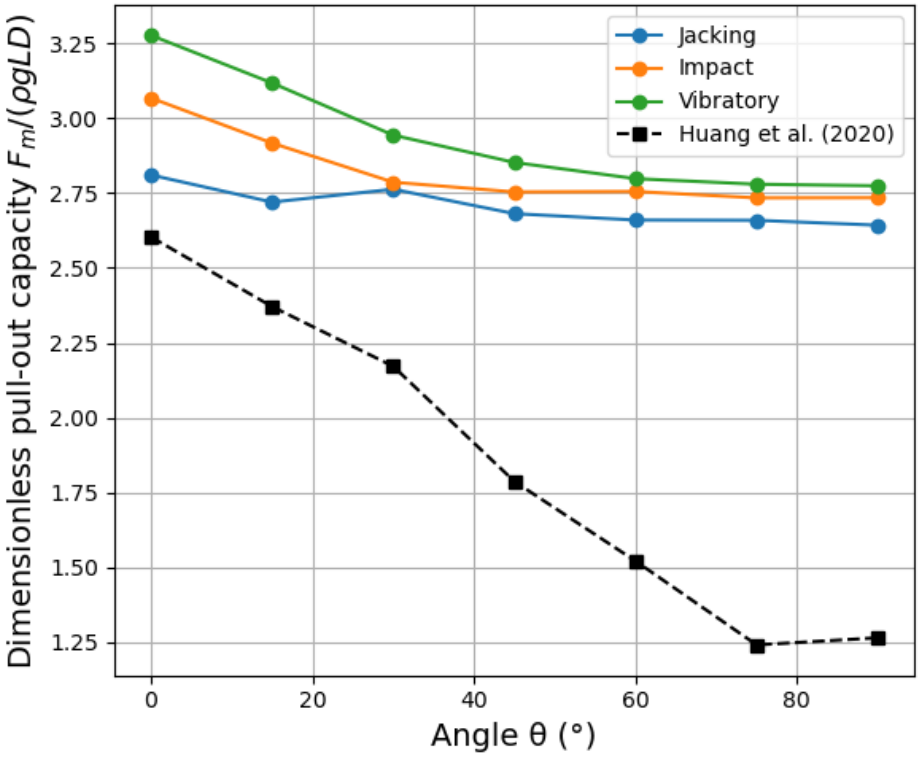

Figure 5.5: Variation of pile capacity with load inclination angles at L/D=0.1

In Figure 5.5, the evolution of pile pull-out capacity with different load inclination angles is shown. From the plot, it is clear that with the increase of the inclination angle, the pull-out capacity decreases, which means that the failure mechanism changes from the combination of soil resistance on both sides of the pile in the horizontal direction to pure shaft friction between the pile and surrounding soil under vertical load. This also matches with the conclusion obtained from previous pile pull-out tests taken by Huang et al. [52]. Moreover, one thing worth mentioning is that, by observing the change in the three curves, the decrease in pull-out capacity for the vibratory driven pile is the most significant, and the jacked pile shows the smallest difference in this decrease. Additionally, in order to prove our research, we compare our results with the centrifuge pile extraction test performed by Huang et al. in 2020

[52]. In their test, they used the same seven inclination pulling angles to extract the model pile in a centrifuge test. The black curve in the plot is obtained from the 'rough' pile results obtained by Huang et al. because in our research the pile is also rough. Comparing the trends of the pull-out capacity development, it can be seen that in the centrifuge test it also shows a decreasing trend, and it is sensitive to the change in inclination angle. The difference in values and the final part of the curve (after 75 degrees) can be explained by the difference in model scale and model properties.

Additional insights into the influence of the load inclination can be obtained by plotting the vertical and horizontal components of the pile pull-out capacity, as shown in Figure 5.6. For all three models, the pull-out capacity components show similar trends. With the decrease of inclination angle, the vertical component of pull-out capacity keeps decreasing, while the horizontal component increases. This means that at lower load inclinations, the vertical pull-out capacity component decreases with the transition to a rigid pile rotation mechanism associated with a laterally loaded pile. Moreover, it is also clear that vibratory driving has the highest pull-out capacity in all inclination angles, while jacking leads to the lowest values. This may be because of the larger amount of soil plug inside the vibratory-driven pile, which means that the inner soil can provide more shaft friction to the pile during the pull-out process, thus making it more difficult to extract the pile from the soil body. Moreover, by comparing our results to the results obtained by Huang et al., a similar development trend can be observed. The vertical pull-out capacity component decreases with a smaller inclination angle, while the horizontal component keeps increasing. Also, in Huang et al.'s results, the horizontal component is also higher than the vertical component; it is caused by the restriction provided by soil in the horizontal direction. The difference in values can be explained by the difference in sample dimension and properties.

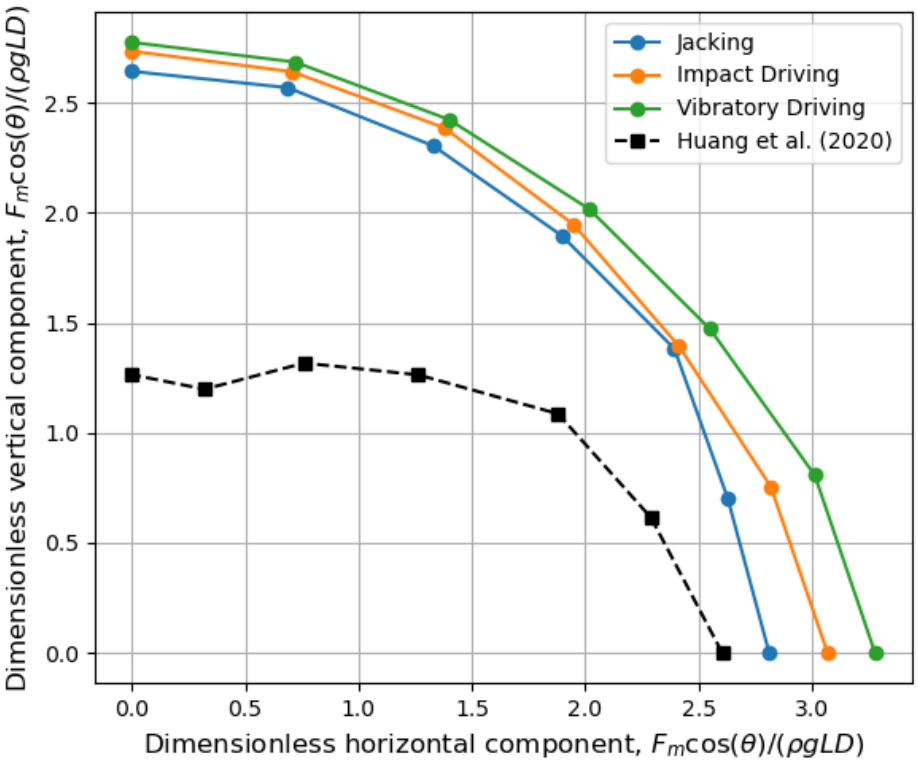

Figure 5.6: Vertical and horizontal components of pile pull-out capacity

5.4. Conclusion

This chapter presented a detailed numerical investigation into the pull-out resistance of open-ended piles installed via jacking, impact driving, and vibratory driving (4 Hz), considering a range of load inclination angles relevant to mooring systems in floating offshore wind turbines. Given the increasing deployment of floating foundations, understanding the tensile behavior of mooring-connected anchor piles under inclined loading is of critical engineering importance.

The simulation results reveal a consistent trend across all installation methods: pull-out capacity decreases with increasing load inclination angle. This reflects a transition in failure mechanism from a combined resistance mobilized by surrounding soil and internal plug (at low angles) to a predominantly shaft friction-controlled behavior under near-vertical tension. Among the three methods, vibratory driving produced the highest pull-out capacities at all angles, attributed to its enhanced soil densification and the formation of more substantial soil plugs, which increased the interface friction and confinement during extraction. Impact driving exhibited intermediate performance, while jacked piles provided the lowest resistance, likely due to their lower degree of internal soil confinement and external densification.

Furthermore, vibratory-driven piles exhibited the greatest sensitivity to load angle, while jacked piles were the least sensitive. This indicates that while vibratory installation enhances overall resistance, it also introduces a more angle-dependent response. The component force analysis further clarified the redistribution of vertical and horizontal pull-out contributions as inclination increased, particularly for vibratory and impact-installed piles. These results were also in good agreement with previous centrifuge model tests by Huang et al. (2020), supporting the validity of the adopted numerical approach.

Moreover, because the pull-out simulation is performed after previous installation stages, there will be influence remaining from installation processes; for example, the pile will have the tendency of moving downwards, which will lead to an unrealistically high reaction force on the connector because it has to withstand the pile from moving downwards. In order to prevent this influence, another stage will be added before pulling out the pile. We call it the 'stabilization' stage, in which we fix the connector while releasing the pile in horizontal, vertical, and rotational directions. After a short period of time, the reaction force on the connector will become stable, and the pull-out simulation can be started.

In summary, the pull-out performance of piles is significantly influenced by both installation history and loading direction. Vibratory driving demonstrates the most favorable resistance characteristics due to its strong densification and plug formation capabilities, making it a promising method for anchoring floating structures subject to large inclined loads. Nevertheless, its higher sensitivity to load directionality suggests that careful consideration should be given to expected load orientations in design. These insights contribute to optimizing foundation strategies for offshore floating wind applications and support further development of installation–performance relationships in geotechnical engineering design.

6

Conclusions and Limitations

6.1. Conclusions

This thesis conducted a comprehensive numerical investigation into the micro-mechanical behavior of open-ended monopiles in soft soil, focusing on the influence of different installation methods and their subsequent pull-out resistance under inclined tensile loading. The primary motivation is to inform and optimize foundation design for offshore wind turbines, particularly in floating configurations where piles are subject to complex loading conditions.

6.1.1. Installation Method Comparison

Chapters 5 systematically compared three widely adopted pile installation methods: jacking, impact driving, and vibratory driving (at 4 Hz and 10 Hz), with respect to their impact on penetration resistance, soil densification, soil plug formation, and surface deformation (uplift or settlement).

- **Penetration Resistance**: Impact driving exhibited the highest resistance due to transient stress wave propagation and localized densification near the pile tip. Jacking produced a smooth and progressive resistance profile, whereas vibratory driving showed the lowest penetration resistance, attributed to reduced effective stress and dynamic softening effects in the surrounding soil.
- **Uplift and Settlement Behavior**: Impact driving caused the most pronounced soil uplift due to its impulsive displacement method, while vibratory driving induced net settlement, particularly at higher frequencies, as a result of enhanced particle rearrangement and soil densification. These observations are crucial for assessing ground surface deformation risks during construction.
- **Soil Plug Formation**: The evolution of plug length ratio (PLR) and incremental filling ratio (IFR) demonstrated that vibratory driving, especially at 10 Hz, generated the longest and most complete soil plugs. In contrast, impact driving resulted in minimal plug development. Given that soil plugs significantly contribute to axial resistance, these differences have direct implications for pull-out performance in anchor pile design for floating foundations.
- **Soil Disturbance and Densification**: Vibratory driving generated the most extensive densification zones around the pile, promoting a denser and more confined soil structure. Jacking produced minimal disturbance with a uniform stress field, whereas impact driving caused intense but localized rearrangement of soil particles.

6.1.2. Pull-out Resistance Analysis

Chapter 6 focused on the tensile pull-out behavior of piles previously installed using the three methods, under load inclination angles ranging from $0°$ to $90°$. This analysis is particularly relevant for the design of anchor piles in floating offshore wind turbines, which are subjected to inclined mooring loads.

- **Inclination Sensitivity**: Pull-out capacity was found to decrease with increasing load inclination angle across all installation methods. This trend is consistent with a shift from combined lateral and axial resistance toward a reliance on shaft friction under vertical loading.

- **Effect of Installation Method**: Vibratory installed piles consistently exhibited the highest pull-out resistance, attributed to dense soil plugs and enhanced shaft friction along the pile-soil interface. Jacked piles showed the lowest resistance, though their force–displacement curves were more stable and less prone to oscillations.
- **Force Component Redistribution**: Analysis of vertical and horizontal components of pull-out capacity revealed that at lower inclination angles, horizontal resistance plays a dominant role. As the angle increases, vertical components become more significant, though total resistance diminishes. Vibratory piles exhibited the greatest variation in force distribution, indicating higher sensitivity to loading direction.

6.1.3. Implications for Offshore Wind Turbine Pile Foundations

The findings from this thesis offer important design insights for both fixed-bottom and floating offshore wind energy systems:

- **Installation Strategy**: Vibratory driving emerges as a highly efficient method for offshore foundation installation, offering lower penetration resistance and improved soil plug development. These attributes facilitate both construction efficiency and long-term tensile capacity, particularly for anchor piles in mooring systems.
- **Performance under Inclined Loads**: The observed decrease in pull-out resistance with increasing inclination angle highlights the importance of considering loading directionality in foundation design. While vibratory driving offers superior overall resistance, its sensitivity to load angle warrants careful application in environments where large load variations are expected.

6.2. Limitations and Future Work

While the numerical study provides comprehensive insights, several limitations exist that could be addressed in future research:

- **Dimensionality**: In this research the dimension of the model is rather unrealistic comparing to the real construction site. For example, the scale of the sample container and the diameter of the pile are pretty small, and the radius of the soil particles are too large comparing real situation, which may cause unrealistic behavior such as extremely long soil plug.
- **Soil Homogeneity**: The soil was modeled as a mono-disperse granular material with simplified properties. Real soils often exhibit heterogeneity, anisotropy, and partial saturation, which influence pile behavior significantly.
- **Effect of Water**: The soil sample in this research is considered as fully drained, which means that the whole process takes place in a dry condition. But in real offshore construction sites, the soil is usually fully saturated, so that the water will cause influence of pile installation and pull out.
- **Pull-out Angles**: In the pull-out simulation, for all the performed pile pull-out tests, the connector starts from the center top of the pile; but in reality the starting position should follow the inclination angle.
- **Vibratory Frequency**: For vibratory driving frequency, only $4Hz$ and $10Hz$ are used in this research. However, for real vibratory driving method, the frequency used is usually around $35Hz$, which is much higher than we used in this research.
- **Soil friction coefficient**: In this research, the friction coefficient of the soil sample is used as 0.1, which is rather small, which will lead to unrealistic behavior such as extremely long soil plug formation.

In light of these limitations, future research can focus on the following aspects:

- Extending the size of the domain, as well as using larger pile diameter and smaller soil particle radius.

- Inclusion of variable soil types (e.g., silty, layered, or cemented soils) to assess installation performance in more complex geologies.
- Investigating the effect of water by using other numerical methods such as CFD-DEM approach.
- Changing the pull-out inclination angles by changing the position of connector in the pull-out simulation.
- Applying higher frequency values as well as more different frequencies to investigate the influence of vibratory frequency.
- Using higher friction coefficient such as 0.2 or 0.3 to investigate the influence of this soil property.

In this research, a 2D DEM model is built to investigate the influence of installation methods. However, in reality, the soil-pile interaction is 3D, which means that there are still differences between this research and real conditions. The biggest difference lies in the nature and number of interparticle contacts. In a 3D system, particles experience nonplanar contact forces and can move out of the plane, leading to a greater number of contacts per particle and a more complex force network. This increases the effective friction at the particle scale, resulting in higher macroscopic friction angles. By contrast, 2D simulations restrict motion and contacts to a plane. For example, in the research of shear flow taken by Fleischmann et al. in 2013, it was reported that 3D DEM simulations accurately predict the peak and residual friction angles observed in experimental tests on sand, whereas 2D DEM simulations tend to significantly underestimate these friction angles [55].

Even though in this research the biggest influence, which is the unrealistic soil behavior under high vibratory frequency, is caused by the friction coefficient; other soil properties such as relative density D_r, shear stiffness G, and grain size distribution will also influence the penetration resistance and pull-out capacity of the pile. A higher D_r results in a denser initial packing, which increases interparticle contact forces during shearing. This would likely lead to higher penetration resistance and greater shaft friction, but it also causes a challenge in simulation time since particle rearrangement becomes more constrained, requiring smaller time steps to maintain numerical stability. The shear stiffness G governs the stress–strain response at small deformations; increasing G would reduce the soil displacement during pile installation. In DEM, this requires careful calibration of contact stiffness to avoid unrealistically stiff responses or excessive computational costs. Grain size and its distribution directly affect the number of contacts per particle and the compressibility of the soil. For example, according to Minh and Cheng (2013), well-graded material is denser and less compressible than evenly graded material [56]. Smaller particles will lead to more contact points, which means that local particle rolling/rearrangement is more difficult. However, using realistic grain size in DEM is computationally demanding because it increases the total number of particles required for a representative volume, thereby greatly extending simulation time. Future investigations that vary D_r, G, and grain size systematically could provide valuable insights into scale effects and material-specific responses, but they will also need to address the associated computational and calibration challenges.

In conclusion, this work reinforces the critical role of installation method and loading conditions in the mechanical performance of offshore monopile foundations. By combining detailed micro-mechanical modeling with parametric analysis, this study contributes to the advancement of performance-based design principles for next-generation offshore energy infrastructure.

Bibliography

[1] M Dolores Esteban et al. “Why offshore wind energy?” In: *Renewable energy* 36.2 (2011), pp. 444–450.

[2] Paul Breeze. *The future of wind power: increasing economic competitiveness as the technology matures*. Business Insights Limited, 2008.

[3] Hannah Ritchie and Pablo Rosado. “Energy Mix”. In: *Our World in Data* (2020).

[4] Shannon Osaka, Rob Bellamy, and Noel Castree. “Framing “nature-based” solutions to climate change”. In: *Wiley Interdisciplinary Reviews: Climate Change* 12.5 (2021), e729.

[5] Ioannis Tsiropoulos et al. “Towards net-zero emissions in the EU energy system by 2050”. In: (2020).

[6] *Offshore renewable energy*. https://energy.ec.europa.eu/topics/renewable-energy/offshore-renewable-energy_en. Accessed: 2024-12-23.

[7] Francesco Valentini, Giulia Fredi, and Andrea Dorigato. “Thermal Energy Storage (TES) for Sustainable Buildings: Addressing the Current Energetic Situation in the EU with TES-Enhanced Buildings”. In: *Natural Energy, Lighting, and Ventilation in Sustainable Buildings*. Ed. by Morteza Nazari-Heris. Cham: Springer Nature Switzerland, 2024, pp. 191–224. ISBN: 978-3-031-41148-9. DOI: 10.1007/978-3-031-41148-9_9. URL: https://doi.org/10.1007/978-3-031-41148-9_9.

[8] Xuefei Wang et al. “A review on recent advancements of substructures for offshore wind turbines”. In: *Energy conversion and management* 158 (2018), pp. 103–119.

[9] Feng Fu. *Design and analysis of tall and complex structures*. Butterworth-Heinemann, 2018.

[10] Muhammad Arshad and Brendan C O’Kelly. “Analysis and design of monopile foundations for offshore wind-turbine structures”. In: *Marine Georesources & Geotechnology* 34.6 (2016), pp. 503–525.

[11] Wei Shi et al. “Load analysis and comparison of different jacket foundations”. In: *Renewable Energy* 54 (2013), pp. 201–210.

[12] Wentao Hu et al. “Response of open-end pipe piles to vertical dynamic load considering the effects of soil plug and soil disturbance during driving”. In: *Soil Dynamics and Earthquake Engineering* 125 (2019), p. 105700.

[13] Xuefei Wang, Xu Yang, and Xiangwu Zeng. “Seismic centrifuge modelling of suction bucket foundation for offshore wind turbine”. In: *Renewable energy* 114 (2017), pp. 1013–1022.

[14] Dominique Roddier et al. “WindFloat: A floating foundation for offshore wind turbines”. In: *Journal of renewable and sustainable energy* 2.3 (2010).

[15] Bryan Puruncajas, Yolanda Vidal, and Christian Tutivén. “Vibration-response-only structural health monitoring for offshore wind turbine jacket foundations via convolutional neural networks”. In: *Sensors* 20.12 (2020), p. 3429.

[16] Rystad Energy. “The state of the European wind energy supply chain”. In: *Industr y Report. Web: WindEurope Market Intelligence Member Area. Accessed: 16th Ju* 2023 (2023).

[17] Zhiyu Jiang. “Installation of offshore wind turbines: A technical review”. In: *Renewable and Sustainable Energy Reviews* 139 (2021), p. 110576.

[18] TAILWIND EU Project. Internal Report. Confidential document. TAILWIND EU Project, 2024.

[19] Jorick Tjaberings, Stefano Fazi, and Evrim Ursavas. “Evaluating operational strategies for the installation of offshore wind turbine substructures”. In: *Renewable and Sustainable Energy Reviews* 170 (2022), p. 112951.

[20] Mark J Kaiser and Brian Snyder. *Offshore wind energy cost modeling: installation and decommissioning*. Vol. 85. Springer Science & Business Media, 2012.

[21] IQIP. *Hydrohammer: Pile Driving Equipment*. Accessed: 29 December 2024. 2024. URL: https://iqip.com/products/pile-driving-equipment/hydrohammer/.

[22] Jack-In Pile. *Jack-In Pile Installation Process*. Accessed: 29 December 2024. 2024. URL: https://www.jackinpile.com.my/services/process.html.

[23] K Rainer Massarsch, Carl Wersäll, and Bengt H Fellenius. "Vibratory driving of piles and sheet piles–state of practice". In: *Proceedings of the Institution of Civil Engineers-Geotechnical Engineering* 175.1 (2022), pp. 31–48.

[24] Martijn Schols. *How Vibratory Hammers are Transforming the Offshore (Wind) Foundation installation market*. https://www.linkedin.com/pulse/how-vibratory-hammers-transforming-offshore-wind-market-schols/. Accessed: 2025-08-06. May 2020.

[25] Lindy Energy. *Floating Wind Turbines: Technology and Potential*. Accessed: 2025-05-29. 2025. URL: https://lindyenergy.com/floating-wind-turbines/.

[26] Erlend Gjelstad Jakobsen and Nikolas Ironside. "Oceans unlocked-a floating wind future". In: *Retrieved from COWI: https://www. cowi. com/insights/oceans-unlocked-a-floating-wind-future* (2021).

[27] Lichen Li et al. "DEM analysis of the sand plug behavior during the installation process of open-ended pile". In: *Computers and Geotechnics* 109 (2019), pp. 23–33.

[28] Nuo Duan et al. "DEM investigation of sand response during displacement pile installation". In: *Ocean Engineering* 230 (2021), p. 109040.

[29] Yihan Bai et al. "Penetration mechanism of open-ended pipe piles under jacking and driving methods". In: *Mechanics of Advanced Materials and Structures* (2024), pp. 1–20.

[30] Lichen Li et al. "DEM analysis of the plugging effect of open-ended pile during the installation process". In: *Ocean Engineering* 220 (2021), p. 108375.

[31] Ning Guo et al. "DEM study of the stress fields around the closed-ended displacement pile driven in sand". In: *Canadian Geotechnical Journal* 61.3 (2023), pp. 549–561.

[32] Jianxue Feng et al. "Performance of Monotonic Pile Penetration in Sand: Model Test and DEM Simulation". In: *Buildings* 14.10 (2024), p. 3327.

[33] Michel Jean. "The non-smooth contact dynamics method". In: *Computer methods in applied mechanics and engineering* 177.3-4 (1999), pp. 235–257.

[34] Frédéric Dubois, Vincent Acary, and Michel Jean. "The Contact Dynamics method: A nonsmooth story". In: *Comptes Rendus Mécanique* 346.3 (2018), pp. 247–262.

[35] Mark Randolph et al. "Challenges of offshore geotechnical engineering". In: *Proceedings of the 16th international conference on soil mechanics and geotechnical engineering*. IOS Press. 2005, pp. 123–176.

[36] ZX Yang et al. "Field behavior of driven prestressed high-strength concrete piles in sandy soils". In: *Journal of geotechnical and geoenvironmental engineering* 141.6 (2015), p. 04015020.

[37] *LMGC90 User Guide*. Comprehensive guidance on using LMGC90. Université de Montpellier. 2012.

[38] Christophe Geuzaine and J-F Remacle. "Gmsh: a three-dimensional finite element mesh generator with built-in pre-and post-processing facilities". In: (2008).

[39] Peter A Cundall and Otto DL Strack. "A discrete numerical model for granular assemblies". In: *geotechnique* 29.1 (1979), pp. 47–65.

[40] Yutaka Tsuji, Toshihiro Kawaguchi, and Toshitsugu Tanaka. "Discrete particle simulation of two-dimensional fluidized bed". In: *Powder technology* 77.1 (1993), pp. 79–87.

[41] Colin Thornton. "Granular dynamics, contact mechanics and particle system simulations". In: *A DEM study. Particle Technology Series* 24 (2015).

[42] Frédéric Da Cruz et al. “Rheophysics of dense granular materials: Discrete simulation of plane shear flows”. In: *Physical Review E—Statistical, Nonlinear, and Soft Matter Physics* 72.2 (2005), p. 021309.

[43] Jean Jacques Moreau. “Some numerical methods in multibody dynamics: application to granular materials”. In: *European Journal of Mechanics-A/Solids* 13.4-suppl (1994), pp. 93–114.

[44] Frédéric Dubois et al. “Lmgc90”. In: *10e colloque national en calcul des structures*. 2011, Clé–USB.

[45] Jean Jacques Moreau and Michel Jean. “Numerical treatment of contact and friction: the contact dynamics method”. In: *Engineering Systems Design and Analysis Conference*. Vol. 4. 1996, pp. 201–208.

[46] Mathieu Renouf, Frederic Dubois, and Pierre Alart. “A parallel version of the non smooth contact dynamics algorithm applied to the simulation of granular media”. In: *Journal of Computational and Applied Mathematics* 168.1-2 (2004), pp. 375–382.

[47] Vincent Acary and Bernard Brogliato. *Numerical methods for nonsmooth dynamical systems: applications in mechanics and electronics*. Springer Science & Business Media, 2008.

[48] Robert Goodell Brown. *Smoothing, forecasting and prediction of discrete time series*. Courier Corporation, 2004.

[49] Berk Turkel et al. “Semiempirical model of vibration-induced ground deformations due to impact pile driving”. In: *Journal of Geotechnical and Geoenvironmental Engineering* 149.11 (2023), p. 04023110.

[50] MF Randolph, R Dolwin, and R Beck. “Design of driven piles in sand”. In: *Geotechnique* 44.3 (1994), pp. 427–448.

[51] F Rausche. “Modeling of vibratory pile driving”. In: *Proceedings of the international conference on vibratory pile driving and deep soil compaction*. 2002, pp. 21–32.

[52] Ting Huang et al. “Drained response of rigid piles in sand under an inclined tensile load”. In: *Géotechnique Letters* 10.1 (2020), pp. 30–37.

[53] Edgar Buckingham. “On physically similar systems; illustrations of the use of dimensional equations”. In: *Physical review* 4.4 (1914), p. 345.

[54] Harvey J Burd et al. “PISA design model for monopiles for offshore wind turbines: application to a marine sand”. In: *Géotechnique* 70.11 (2020), pp. 1048–1066.

[55] JA Fleischmann, ME Plesha, and WJ Drugan. “Quantitative comparison of two-dimensional and three-dimensional discrete-element simulations of nominally two-dimensional shear flow”. In: *International Journal of Geomechanics* 13.3 (2013), pp. 205–212.

[56] NH Minh and YP Cheng. “A DEM investigation of the effect of particle-size distribution on one-dimensional compression”. In: *Géotechnique* 63.1 (2013), pp. 44–53.